THE ASTROPHYSICAL JOURNAL, 492:617–634, 1998 January 10
© 1998. The American Astronomical Society. All rights reserved. Printed in U.S.A.

PHOTOMETRIC AND SPECTROSCOPIC OBSERVATIONS OF A DIFFUSE INTERSTELLAR FILAMENT IN THE FOREGROUND OF THE MAGELLANIC CLOUDS

BRYAN E. PENPRASE,[1,2] JENNIFER LAUER,[3] AND JOEL AUFRECHT
Department of Physics and Astronomy, Pomona College, Claremont, CA 91711

AND

BARRY Y. WELSH[1]
Experimental Astrophysics Group, Space Sciences Lab, University of California at Berkeley, Berkeley CA 94720
Received 1996 September 4; accepted 1997 August 12

ABSTRACT

We report the results of a photometric and spectroscopic study of stars that appear toward an infrared bright filament in the region between the LMC and SMC in the constellation Mensa. The filament was chosen for study because of its large angular size, intense IR emission, and proximity to an X-ray source observed using *ROSAT*. We have observed 38 stars in the vicinity of the filament with combined *uvby*-Hβ photometry, and nine stars with a high-resolution spectrograph ($\lambda/\delta\lambda > 70{,}000$) in the wavelength of the Na I D lines. For two stars, we present high-dispersion Ca II K line absorption spectra from the filament. We have derived a distance estimate of 230 ± 30 pc for the filament, and a mean color excess $E(B-V) = 0.17 \pm 0.05$ mag. The resulting extinction toward the cloud is $A_V = 0.53$ mag, assuming $R_V = 3.1$. The Na I D line profiles are strongly saturated for stars at distances of $d \geq 200$ pc, and fits to the profiles trace multiple components with $v_{\rm LSR} = 0.0$ km s^{-1} to $v_{\rm LSR} = 10$ km s^{-1} and *b*-values ranging from 1.0 km s^{-1} $< b <$ 3.5 km s^{-1}. We observe strikingly different Ca II absorption line profiles in the spectra of two of the background stars. The sight line toward HD 22252 has at least seven separate components of Ca II absorption, while the sight line toward HD 26109 appears to have only a single component. The spectroscopic results suggest that the warm gas component of the filament traced by Ca II has highly variable kinematics from one end to the other, perhaps as a result of shock excitation. Examination of *IRAS* colors for the cloud reveals values of *R*(12, 100) and *R*(60, 100) enhanced by more than a factor of 2 at the high galactic latitude end of the cloud near the HD 22252 sight line and near the center of the cloud, which could arise from shock-heated dust grains. By combining our distance estimate with the *ROSAT* X-ray intensity, we can derive an estimate of the hot gas density in the local bubble of $n_e = 3.47 \times 10^{-3}$ cm^{-3}. The IR filament appears to offer an excellent laboratory for probing a wide range of interstellar conditions within a single diffuse interstellar cloud. At the estimated distance of 230 pc and with its Galactic coordinates of (290, −43), it is also possible that the filament could have been formed from the Geminga supernova; further observations are needed to confirm this possibility.

Subject headings: dust, extinction — ISM: clouds — ISM: individual (anon)

1. INTRODUCTION

Spectroscopic observations of the LMC and its surroundings have been obtained in recent years in the wavelengths of Ca II (Wayte 1990), with *IUE* (Blades & Panagia 1989; Blades et al. 1988), and in high-resolution observations of Na I (De Boer et al. 1987) and Ti II (Caulet 1996; Albert et al. 1993). These observations have concentrated on the abundances and kinematics of the LMC clouds, and have identified several intermediate-velocity components at velocities of $v_{\rm LSR} = 60$ km s^{-1}, $v_{\rm LSR} = 130$ km s^{-1}, and $v_{\rm LSR} = 170$ km s^{-1}, as well as a very strong component near $v_{\rm LSR} = 0$ km s^{-1}. The intermediate- and low-velocity material in the foreground of the Magellanic Clouds is usually considered to be of galactic origin, and little attention has been paid to the morphology and kinematics of these interstellar components.

The region between the LMC and SMC has been mapped in 21 cm (Coulomb, Poppel, & Heiles 1977), who observed a large "semicircular arc" with a strong peak in emission between 0 and 8 km s^{-1}. This feature had been detected previously in Hα emission (de Vaucouleurs 1960), and a second optical study attempted to measure the polarization of stars near the filament (Luna & Testori 1988), but the distance of the filament, its origin, kinematics, and any possible relation to the LMC and the Magellanic stream remained unknown. In the infrared, the filament is a very strong feature that appears as an arc of strong emission transverse to a line connecting the LMC and SMC (see Fig. 1). Owing to the low dust content of the Magellanic Stream (Fong et al. 1987), the strong IR and optical emission from the filament suggests a local galactic origin, but direct detection from extinction or absorption by the filament or sources of known distance has not been previously reported.

Early 21 cm observations of the region between the LMC and SMC revealed further hints of foreground filamentary emission (Mathewson et al. 1979). A more recent 21 cm study of the filament was conducted (McGee et al. 1986) in which the filament was observed with 15′ resolution at pointings determined by the structure revealed in *IRAS* emission. The 21 cm spectra detected strong H I emission at

[1] Visiting Astronomer, Cerro Tololo Inter-American Observatory. CTIO is operated by AURA, Inc. under contract to the National Science Foundation.

[2] Visiting Astronomer, European Southern Observatory, La Silla, Chile.

[3] Present address: University of Minnesota, Department of Astronomy and Astrophysics, 116 Church Street SE, Minneapolis, MN 55455.

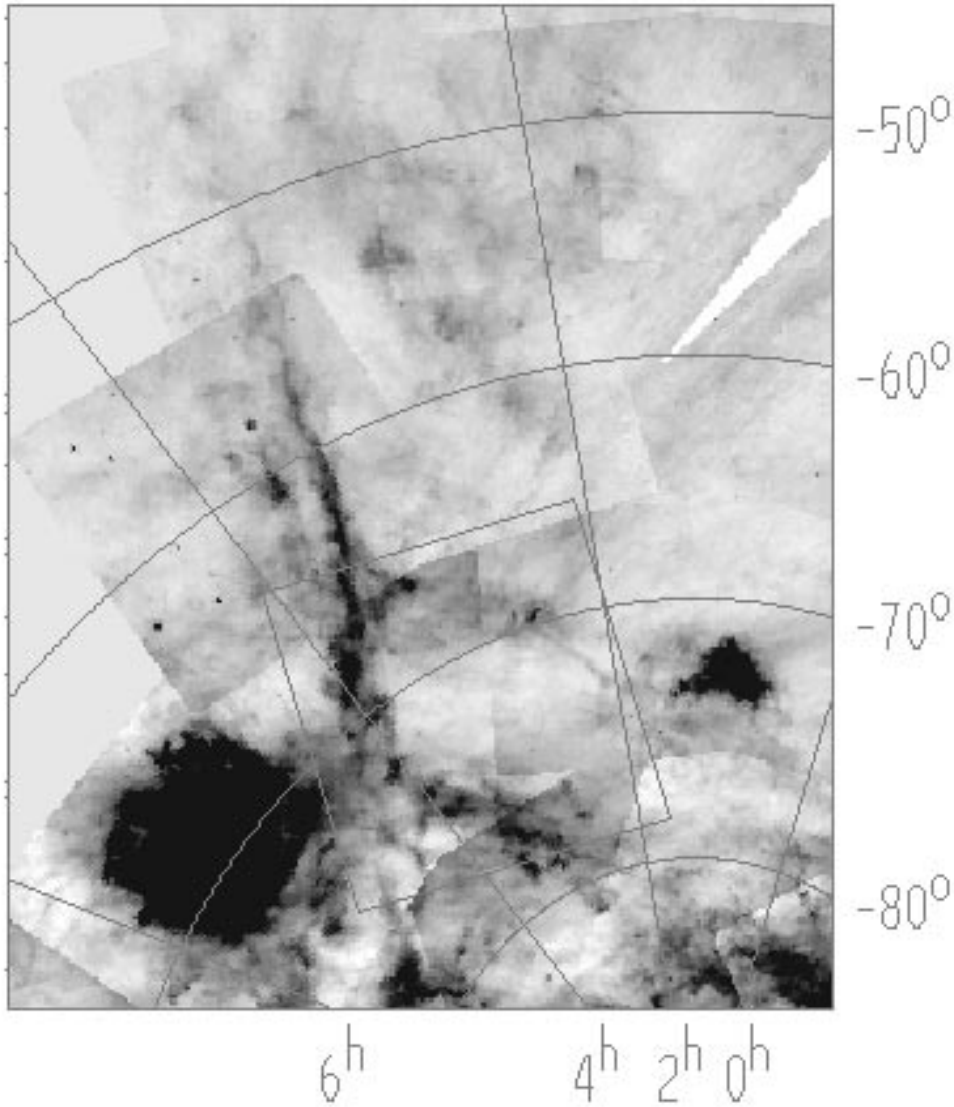

FIG. 1.—*IRAS* 100 μm mosaiced image of the LMC and SMC, showing the large filament that is the subject of the present work. The image shows over 12 *IRAS* ISSA sky flux plates that have been flattened using an algorithm to remove a planar fit to the zodiacal background residuals. Mismatches on the plate boundaries are a result of slight curvatures in the zodiacal background residuals. Box indicates the region studied in detail.

3–5 km s^{-1}, with a half-width of 7.0 km s^{-1}. These authors also note that the emission from the filament appears to trace a great circle, with the northern half of the emission exhibiting a radial velocity gradient from $+1.7$ km s^{-1} to $+11.1$ km s^{-1}, and the southern half showing a more constant radial velocity of 3.5 km s^{-1}. The authors interpret this gradient as indicating two "streams" of material. In both streams, however, the observed line widths are very similar at 7 km s^{-1}, and the observed values of $B_{100\mu}/N_{\rm H}$ for both streams are low, with $B_{100\mu}/N_{\rm H} = 0.74 \times 10^{-14}$ Jy Sr^{-1} (H atom cm^{-2})$^{-1}$, much lower than the average value for galactic cirrus, $B_{100\mu}/N_{\rm H} = 1.4 \times 10^{-14}$ Jy Sr^{-1}(H atom cm^{-2})$^{-1}$ (Boulanger et al. 1985). From these observations, it seems clear that the filament has no connection with the LMC and Magellanic stream other than angular proximity, and while of galactic origin, is at an unknown distance.

In the present work, we have detected the filament optically, using measurements of photometric extinction and optical absorption of background stars to provide a better idea of its extent, distance, and possible origin. An additional motivation for the present work comes from recent *ROSAT* observations of X-ray "shadows" of local molecular clouds. Knowledge of the distance and extinction of the absorbing clouds can be combined with the *ROSAT* X-ray shadowing data to test models of the diffuse X-ray background, which will improve our knowledge of the local interstellar medium (Guo et al. 1995; Burrows & Mendenhall 1991). The IR filament studied in the present work has been detected in absorption in the wavelengths of 0.1–0.3 keV using the *ROSAT* PSPC (Wang & Yu 1994). Using a mean value for the Galactic hot gas density of $n_e = 6.3 \times 10^{-3}$ cm^{-3}, Wang & Yu (1994) estimated a distance of 70 pc for the IR filament examined in the current work. This distance estimate is very uncertain, since it assumes that both the hot gas density and the filling fraction are constant throughout the Galaxy in order to invert the observed emission measure to determine the cloud distance. Any resulting modifications of the distance estimate to the cloud would have a direct impact on the estimated hot gas density of the Local Bubble near the filament (Q. D. Wang 1994, private communication).

In order to investigate this possibility in more detail, we

obtained photometric observations of 38 stars toward the densest part of the cloud and high-resolution spectroscopic observations of early-type (A and B) stars that appear toward the filament. The photometric extinction for stars at increasing distances toward a cloud has been used effectively for many years to determine distances to interstellar features (Franco 1992; Penprase 1992). The spectroscopic observations can also provide kinematic information about the filament that can be compared with H I maps to determine whether the cloud has been detected in absorption.

One possible explanation for the formation of the filament toward the LMC may be that it is an old supernova remnant. Several features in the local interstellar medium, such as the North Polar Spur and other shells of gas (Heiles 1989; Heiles et al. 1980; Frisch 1981) appear to have been formed from supernova events. Observations of the Geminga pulsar (Gehrels & Chen 1993) have suggested that the Local Bubble may be the result of a recent supernova that detonated at a distance of approximately 60 pc from the sun, and that many of the largest features of the ISM may have been formed by shocks from the local supernova. The possibility of this filament arising from a supernova is discussed in § 4 of the present work.

2. OBSERVATIONS

2.1. *Photometric Observations*

Photometric observations of our program stars were made using the CTIO 1 m telescope during two nights in 1993 March. The ASCAP photometer and S-20 photomultiplier tube were used with the standard CTIO *uvby* and Hβ filter set. We observed 91 stars during the night of 1993 March 3; 16 stars were observed during the first half of the night of 1993 March 4 to check the results of the first night observations. We observed each of our program stars at least twice in each filter, and rejected observations with large discrepancies between repeat measurements with the same filter. During each night, at least 25% of the observing time was devoted to standard star observations, and for the first night we used 32 separate observations of standard stars. The observing conditions were photometric during both nights, although some cirrus arrived during the second half of the second night, after our observations were finished. The standard star *uvby* and Hβ colors were taken from the papers of Olsen (1983) and Gronbech & Olsen (1976).

The extinction coefficients were determined by plotting the differences between standard star instrumental magnitudes as a function of airmass. The extinction corrections were based on standard star observations taken at airmasses ranging from $1.0 \leq \sec z \leq 2.0$. The typical airmass of our program star observations was $\sec z = 1.5$. The observations were converted into standard magnitudes using a modified version of a FORTRAN routine that calculates extinction corrections, transformation coefficients, and background rates (H. Bond 1992, private communication). The average residuals σ_i for the standard star observations were (in magnitudes) $\sigma_v = 0.054$, $\sigma_{b-y} = 0.015$, $\sigma_{m_1} = 0.021$, and $\sigma_{c_1} = 0.29$. The large residuals for c_1 are due to the fact that c_1 depends on the u filter, and our program stars had little flux in this wavelength range. The extinction and distance estimates used only the v, $b - y$, m_1, and Hβ magnitudes, and therefore were not affected by the measurements of c_1. Comparison of the observed values from the two nights showed agreement consistent with the above residuals.

The Hβ magnitudes were converted from the instrumental values using a least squares fitting program written in IDL. The observed standard star magnitudes were fitted to the published magnitudes of stars from Groenbeck & Olsen (1976), and the fitting constants were then used to derive standard Hβ magnitudes for the program stars. The residuals between the fit and the observed Hβ magnitudes for the Groenbeck & Olsen (1976) stars suggest that our technique is accurate to within ± 0.01 mag in Hβ. Stellar parameters and the observed values from the *uvby*-Hβ photometry are presented in Table 1.

Photometric MK temperature classifications were performed for the stars using a procedure based on main-sequence fitting of reddening-free color indices (Penprase 1992). Spectral types were determined using both Hβ and the photometric index $[m_1]$ (Mihalas & Binney 1981), where $[m_1] = m_1 + 0.18(b - y)$. We used a main-sequence calibration of the $[m_1]$ and Hβ indices to determine the intrinsic colors of the stars in our sample. Standard stars provided a locus of values of $[m_1]$ and Hβ for the main sequence, and for each of our program stars we found the closest point on the main sequence in the $[m_1]$-Hβ plane. The distance between the $[m_1]$ and Hβ values of the star and the main sequence also gave a measure of the uncertainty in the measurement. The results of the photometric spectral classification are presented in columns 4–6 of Table 2.

For most of the stars, the measured values of Hβ and $[m_1]$ agreed well with our fitted main sequence. However, the observed values of a few stars did not obviously correspond to a particular main-sequence spectral type. Those stars have been flagged in Table 1, and could represent either peculiar stars or spectroscopic binary stars. The calculated spectral types were compared with MK spectral types available from the SIMBAD database. Most of the calculated spectral types agreed to within two temperature subclasses with the SIMBAD MK types. Figure 2 shows a graphical comparison of the MK temperature classes determined from photometry with those in the literature. An analysis of the residuals from Figure 2 gives a mean uncertainty of 2.5 temperature classes in the photometric classification, which is consistent with those found by Penprase (1992). If peculiar stars flagged in Table 1 are excluded, the

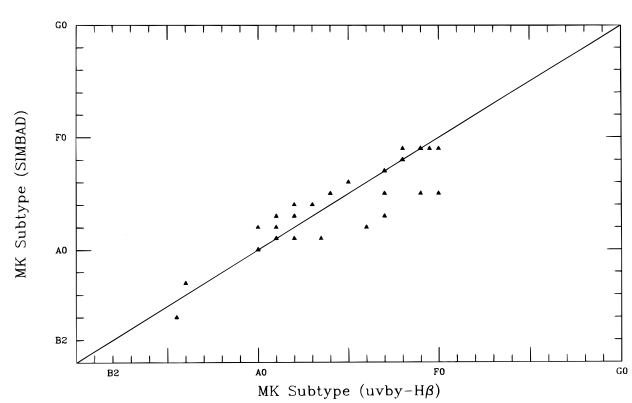

FIG. 2.—A comparison of the MK temperature subtypes derived from photometric classification (x-axis) with those in the literature and found with the SIMBAD database (y-axis). Analysis of the disagreement between the two suggests that the photometric classification is generally accurate to within two MK temperature subclasses.

TABLE 1

STELLAR COORDINATES AND OBSERVED PHOTOMETRY

Number	Star Name	α(1950)	δ(1950)	v	$b-y$	m_1	c_1	Hβ
1	HD 17419	2:43:06.7	−69:46:43	9.39	−0.05	0.08	0.33	2.701
2	HD 17732	2:46:09.9	−69:17:27	9.68	0.15	0.24	0.82	2.826
3	HD 17901	2:47:51.5	−69:02:36	9.81	0.13	0.18	0.95	2.852
4	HD 17981	2:48:41.3	−70:25:30	8.41	0.19	0.20	0.87	2.761
5	HD 20966	3:18:29.8	−65:54:29	7.32	0.08	0.20	0.90	2.867
6	HD 21115	3:19:55.0	−65:57:56	7.26	0.19	0.17	0.69	2.747
7	HD 22218	3:30:12.2	−65:19:39	8.78	0.18	0.21	0.74	2.769
8	HD 22252	3:30:20.4	−66:39:31	5.81	0.00	0.10	0.70	2.717
9	HD 22449	3:30:47.9	−74:45:50	7.51	0.07	0.19	1.07	2.868
10	CPD −65°249	3:31:39.7	−65:19:54	10.31	0.18	0.19	0.73	2.752
11	HD 22488	3:32:16.9	−66:53:47	7.52	0.22	0.20	0.73	2.766
12	CPD −75°239	3:33:47.6	−75:33:06	10.28	0.05	0.03	0.55	2.702
13	HD 23334	3:39:34.3	−67:23:27	9.20	0.05	0.16	1.33	2.864
14	HD 23509	3:41:02.6	−66:38:10	7.73	0.17	0.21	1.15	2.797
15	CPD −67°248	3:41:09.4	−66:53:19	9.29	0.15	0.22	1.09	2.830
16	CPD −74°277	3:51:45.0	−74:44:35	10.23	0.23	0.18	1.09	2.808
17	CPD −66°227	3:53:01.3	−66:39:23	10.06	0.15	0.16	1.17	2.896
18	HD 25027	3:53:21.0	−70:19:15	9.36	0.23	0.13	1.05	2.793
19	HD 25224	3:54:30.9	−73:44:19	9.33	0.23	0.15	1.04	2.784
20	CPD −70°268	3:54:56.3	−69:51:23	9.84	0.27	0.23	0.92	2.730
21	HD 25863	3:59:34.6	−74:53:12	9.89	0.20	0.13	1.29	2.853
22	HD 25938	4:01:00.5	−71:18:20	6.54	0.03	0.19	1.39	2.898
23	HD 26109	4:02:34.5	−70:24:33	8.54	0.09	0.13	1.50	2.897
24	CPD −68°242	4:04:07.2	−68:02:29	11.17	0.26	0.19	1.01	2.694
25	CPD −72°278	4:05:12.6	−72:00:51	10.00	0.11	0.20	1.42	2.856
26	HD 26433	4:05:35.4	−69:32:03	9.49	0.24	0.15	1.24	2.779
27	HD 26594	4:06:26.8	−73:24:50	8.91	0.15	0.18	1.27	2.868
28	HD 26541	4:06:30.5	−70:22:37	9.77	0.12	0.19	1.42	2.939
29	HD 26668	4:06:43.4	−75:39:48	9.42	0.18	0.22	1.06	2.757
30	HD 27143	4:11:44.0	−70:52:01	9.24	0.22	0.16	1.00	2.764
31	CPD −71°252	4:11:45.7	−71:15:36	10.17	0.23	0.20	1.01	2.731
32	HD 27346	4:13:29.5	−70:32:46	6.91	0.21	0.17	1.11	2.762
33	HD 27503	4:15:08.0	−69:39:30	10.51	0.13	0.12	1.52	2.893
34	HD 270501	4:26:00.6	−73:13:48	10.03	0.20	0.21	1.09	2.829
35	HD 28722	4:26:06.2	−71:23:54	9.84	0.14	0.17	1.52	2.878
36	HD 29769	4:35:21.8	−72:50:07	6.97	0.12	0.18	1.39	2.829
37	HD 29921	4:37:03.3	−71:47:31	8.84	0.22	0.18	1.32	2.805
38	HD 30580	4:42:36.3	−73:37:26	8.89	0.16	0.17	0.78	2.803

NOTE—All the coordinates data are from the SIMBAD database; the CPD star number refers to its SIMBAD designation.

average residual between calculated and SIMBAD classification is 1.35 temperature subclasses.

2.2. *Spectroscopic Observations*

Spectroscopic observations of the clouds were obtained during three separate observing runs. We used the 1.5 m telescope of the Cerro Tololo Inter-American Observatory with the bench-mounted echelle spectrograph during three nights of 1993 February. The spectroscopic observations were part of a survey to search for high-velocity clouds in absorption. The spectrograph was used at a resolving power of $\lambda/\delta\lambda = 70{,}000$ at the Ca II K wavelength of 3933.66 Å. The stars HD 22252 and HD 26109 were observed at CTIO during the first observing run. A second observing run was conducted during 1994 July using the Coude Auxiliary Telescope (CAT) and the 3.6 m Coude Echelle Spectrograph (CES) of the European Southern Observatory. The spectrograph was used with the long camera and the remote observing facility of ESO at Garching to control the CAT telescope. During the second run, the star HD 22252 was observed at the highest single-pass resolving power possible ($\lambda/\delta\lambda = 130{,}000$) with the CAT and CES, in order to resolve what appeared to be multiple components in the spectrum from the first observing run.

Additional spectroscopic observations at the Na I D line wavelengths of 5889.95 Å and 5895.92 Å were obtained using the 1.5 m bench-mounted echelle spectrograph during a run in 1997 January. These spectra were obtained with a resolving power of $\lambda/\delta\lambda = 70{,}000$ and had typical S/N ≥ 40. The Na I D spectra were obtained in order to trace the extent of the cloud, and to help verify its photometric detection.

2.3. *Spectroscopic Data Processing*

The spectroscopic data were processed using the standard NOAO IRAF analysis package. Customized IRAF routines written by one of us (B. E. P.) were used to optimize modeled column densities and *b*-values, and to correct the observed velocities to LSR velocities. The CCD frames were corrected for fixed pattern noise, cosmic ray, and dark count backgrounds, and were fitted onto a wavelength scale using the IRAF spectroscopy routines.

Line profile modeling of the high-resolution spectrum of HD 22252 was performed using the XVOIGT package by David Mar of the University of Sydney (Mar & Bailey 1995). With this package, the user manually adds and modifies model clouds to produce a calculated profile to simulate the observed absorption line profile. With the resolving power of $\lambda/\delta\lambda = 136{,}000$, it was possible to distinguish additional components that were unresolved in the

TABLE 2

QUANTITIES DERIVED FROM THE PHOTOMETRIC OBSERVATIONS

Number	Star Name	Hβ	$[m_1]$	Spectral Type	M_v	$(B-V)_0$	$(B-V)$	$E(B-V)$	r_1[a] (pc)	r_2[b] (pc)
1	HD 17419	2.701	0.07	B5.5	-0.07	-0.15	-0.10	0.05	725	...
2	HD 17732	2.826	0.27	A6[c]	2.64	0.17	0.25	0.09	225	...
3	HD 17901	2.852	0.20	A4	2.33	0.11	0.22	0.11	270	...
4	HD 17981	2.761	0.23	A9.5	3.09	0.29	0.30	0.01	110	350
5	HD 20966	2.867	0.22	A3[c]	2.15	0.09	0.13	0.05	100	105
6	HD 21115	2.747	0.20	F0	3.15	0.31	0.31	0.00	65	85
7	HD 22218	2.769	0.24	A9	3.03	0.27	0.30	0.03	140	...
8	HD 22252	2.717	0.10	B6	0.014	−0.14	−0.01	0.13	120	260
9	HD 22449	2.868	0.20	A2.5	2.06	0.08	0.13	0.05	110	150
10	CPD −65°249	2.752	0.23	F0	3.148	0.31	0.30	−0.01	275	...
11	HD 22488	2.766	0.24	A9	3.03	0.27	0.35	0.08	70	200
12	CPD −75°239	2.702	0.04	B5.5	−0.07	−0.15	0.10	0.25	820	...
13	HD 23334	2.864	0.17	A1	1.73	0.03	0.10	0.07	280	230
14	HD 23509	2.797	0.24	A7.5	2.84	0.21	0.28	0.07	90	215
15	CPD −67°248	2.830	0.25	A5.5	2.56	0.15	0.26	0.10	190	215
16	CPD −74°277	2.808	0.22	A7	2.77	0.19	0.37	0.18	240	...
17	CPD −66°227	2.896	0.18	A1.5	1.85	0.04	0.25	0.21	320	...
18	HD 25027	2.793	0.17	A7.5	2.84	0.21	0.36	0.15	160	...
19	HD 25224	2.784	0.20	A8	2.9	0.23	0.36	0.13	160	...
20	CPD −70°268	2.730	0.27	F1	3.27	0.34	0.42	0.09	180	...
21	HD 25863	2.853	0.17	A1	1.73	0.03	0.32	0.29	280	...
22	HD 25938	2.898	0.19	A1.5	1.85	0.05	0.06	0.02	80	100
23	HD 26109	2.897	0.14	A0	1.48	0.00	0.17	0.17	200	230
24	CPD −68°242	2.694	0.24	A3	3.55	0.09	0.40	0.32	210	...
25	CPD −72°278	2.856	0.22	A3.5	2.24	0.09	0.20	0.11	300	...
26	HD 26433	2.779	0.19	A8.5	2.96	0.25	0.38	0.13	170	...
27	HD 26594	2.868	0.20	A2.5	2.06	0.08	0.25	0.17	180	230
28	HD 26541	2.939	0.22	A1.5[c]	1.85	0.05	0.20	0.15	310	...
29	HD 26668	2.757	0.25	F0	3.15	0.31	0.30	−0.01	180	...
30	HD 27143	2.764	0.20	A9	3.03	0.27	0.34	0.07	160	...
31	CPD −71°252	2.731	0.24	F1	3.27	0.34	0.36	0.02	230	...
32	HD 27346	2.762	0.20	A9.5	3.09	0.29	0.33	0.04	55	115
33	HD 27503	2.893	0.15	A0.5	1.16	0.02	0.22	0.20	550	...
34	HD 270501	2.829	0.25	A5.5	2.57	0.15	0.33	0.18	240	...
35	HD 28722	2.878	0.19	A2[c]	1.95	0.06	0.23	0.17	300	540
36	HD 29769	2.829	0.20	A5.5	2.57	0.15	0.20	0.05	70	260
37	HD 29921	2.805	0.22	A7	2.77	0.19	0.34	0.15	130	...
38	HD 30580	2.803	0.19	A7	2.77	0.19	0.26	0.07	150	...

[a] Distances to program stars based on zero-age main sequence colors and a value of $R_v = 3.2$.
[b] Distances to program stars based on *HIPPARCOS* parallaxes.
[c] Possible peculiar star; see § 2.1.

$\lambda/\delta\lambda = 70{,}000$ spectrum. The higher resolution corresponds to an instrumental FWHM of 2.2 km s^{-1}, matching the expected thermal b-value of 1.38 km s^{-1} for gas at 4600 K. The instrumental resolution is expected to be close to the widths of the absorbing components, which are broadened by both thermal and turbulent motions (see § 3.2). Line profile modeling was performed by adjusting the Gaussian line width parameter b, column density N, and LSR velocity $v_{\rm LSR}$ for each cloud until the residual between the observed data and the model was minimized. The number of components and the resulting parameters were chosen from a visual evaluation of the residual that was plotted simultaneously with the modeled profile. To ensure that adopted b-values were consistent with our resolution, we limited the minimum possible modeled b-value to equal or greater then the instrumental resolution of 1.38 km s^{-1}. While the line profile models are not unique, we tried to use the simplest model possible to recreate the observed profile with rms residuals smaller than the expected noise level. We estimate the uncertainty in our modeled b-values to be within 0.5 km s^{-1}, and column densities to be accurate to within 10%.

To check the quality and consistency of the data, we compared the equivalent widths of the HD 22252 sight line derived from the high-resolution ESO spectrum and the medium-resolution CTIO spectrum. We found that the total equivalent width W_λ(Ca II) of the two spectra agreed to within 15%. We measured an equivalent width from the ESO spectrum of W_λ(Ca II) = 105 mÅ, while the value from the CTIO spectrum was slightly higher, at W_λ(Ca II) = 119 mÅ. The total column densities for the two spectra were in excellent agreement, and independent reductions for the two HD 22252 spectra yielded total column densities of $N_{\rm Ca\,II} = 1.52 \times 10^{12}$ cm^{-2} for the CTIO spectrum, and $N_{\rm Ca\,II} = 1.55 \times 10^{12}$ cm^{-2} for the higher resolution ESO spectrum. We also checked our line profile modeling results by fitting the high-resolution profile with both XVOIGT and a modified version of the IRAF routine SPLOT, which calculates column densities. Both estimates agreed to within 10%. The LSR velocities from the observations at CTIO and ESO also agreed well, and the common component velocities agreed to within 0.5 km s^{-1}.

The second set of CTIO spectra in the Na I D line wavelengths were fit with a second custom IRAF routine program, an iterative fitting algorithm that performs simultaneous fits of both D1 and D2 line components using a Voigt profile model convolved with a Gaussian instrumental response function. The cloud models were selected based on a minimization of the observed χ^2 between the data and

fit. The simultaneous fitting routine makes use of the different oscillator strengths of the two components to determine accurate b-values based on a curve of growth. The results made it possible to determine that several of the lines were saturated, but with b-values well below our instrumental resolution. These results are presented in § 3.4.

3. RESULTS

3.1. *Photometric Spectral Classification of Stars*

Figure 3 shows an Infrared Sky Survey *IRAS* 100 μm image of the cloud, with the positions of the program stars indicated. The numbers labeled in Figure 3 correspond to the line numbers of the star in Table 1. The stars chosen were of spectral types F and earlier, to allow for the determination of the reddening toward the filament. All the stars were observed in the *uvby*-Hβ system, and the photometric results for the program stars are presented in Table 1. Examination of Figure 3 immediately reveals the high degree of spatial inhomogeneity in the cloud, suggesting that many separate cloudlets coexist in the region, possibly with wide ranges of extinction.

To help estimate the extinction in the cloudlets, we have used our Strömgren photometry to estimate the color excesses for the stars. From the assigned spectral types of our program stars, we determined $(B-V)_0$ and M_V for each of the stars. The $(B-V)_0$ index was assigned based on values from Zombeck (1990), and the M_V values were assigned from an interpolation of ZAMS values from Zombeck (1990). The ZAMS M_V values reflect slightly less luminous stars, allowing us to provide a lower limit to stellar distances based on photometric spectral classifications. In addition, we converted our measured values of $(b-y)$ to $(B-V)$, using the transformation coefficients found in Penprase (1992). From the converted $b-y$ observations and estimated $(B-V)_0$, we have derived values of $E(B-V)$ for the stars in the region, presented in column 8 of Table 2. Table 2 also lists the estimated values of MK spectral subclass, and the resulting values of M_V and $(B-V)_0$ in columns 5 and 6. The derived values of A_V are in the range $0.0 \leq A_V \leq 0.5$ for the stars toward the cloud.

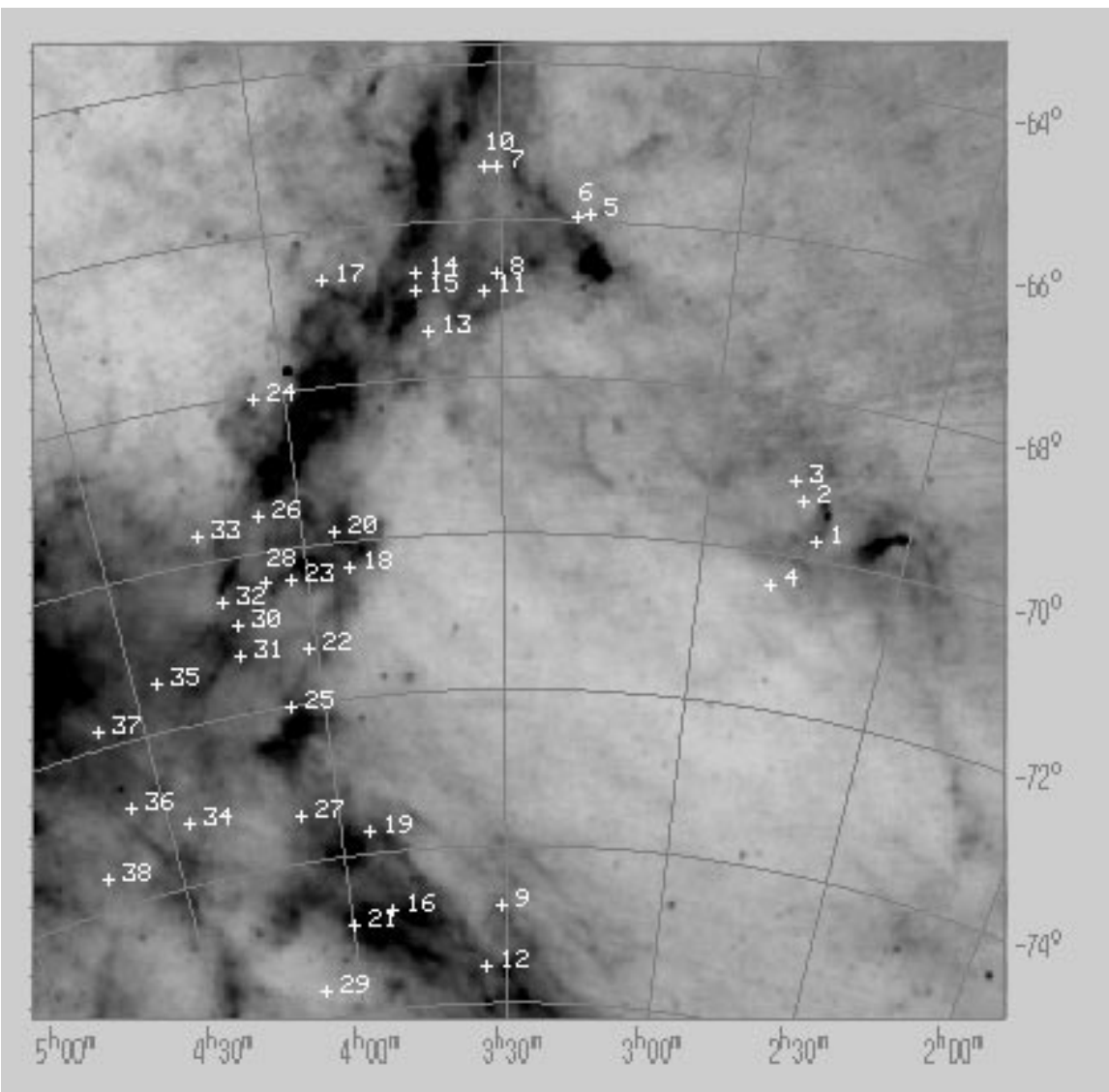

FIG. 3.—*IRAS* 100 μm image of the region studied in the present work, with the locations of the stars in Table 1 indicated. Numbers correspond to the line number of the star in Table 1. The sample of stars is chosen to match the IR contours of the clouds in order to maximize the chance of detecting the extinction in the filament.

Strömgren photometry has been shown to be accurate in determining the intrinsic colors of observed stars (Heck & Mersch 1980), but less effective in determining the luminosity of stars. It is therefore difficult to determine distances from photometry with certainty. For each of the stars, however, it is possible to determine distance based on the main-sequence luminosity at the estimated temperature class. This approach will produce a lower limit to the stellar distance. Assuming that our sample of A and F stars is likely to be mostly of luminosity class V, we can use trends in $E(B-V)$ against class V distance to estimate the distance of clouds, in a manner similar to a Wolf diagram, where the discontinuity in a plot of $E(B-V)$ against distance results from the absorption of the cloud (Scheffler & Elsasser 1987). However, the intrinsic uncertainties in photometric distance determinations lead us to take the photometric estimates with caution because of the unknown luminosity classes. Whenever possible, we have used new parallax data from the *HIPPARCOS* satellite for our distance determinations, and these distances are included in Tables 2 and 3 below.

3.2. *Variation in $E(B-V)$ as a Function of Stellar Distance*

A plot of $E(B-V)$ against distance for all our program stars, using distances derived from photometric classification, is presented in Figure 4*a*. Several deviant points exist in Figure 4*a*, but the mean extinction of the program stars does increase significantly at distances beyond 200 pc, and levels off to an average value of $E(B-V) = 0.15$ for $d \geq 230$ pc.

Several points appearing in Figure 4*a* at significant distances show little or no color excess, and we believe that these stars appear toward "holes" in the filament. The high degree of spatial inhomogeneity in the cloud is visible in Figure 3, with patchiness on scales in the limiting *IRAS* resolution of 10′, and these holes could give rise to some of the scatter visible in Figure 4*a*. For example, the extinction toward the stars CPD $-65°249$ and CPD $-71°252$ appears very small despite apparent stellar distances of 275 and 230 pc.

To test whether the low extinction sight lines appear toward "holes" in the filament, we extracted images for 12 arcminute square regions centered on these two stars, along with two fields toward more highly reddened stars (CPD $-66°227$, $E(B-V) = 0.21$; HD 25863, $E(B-V) = 0.29$) and two fields in "empty" regions far from the filament, centered at (3^h15^m, $-69°$) and (3^h15^m, $-69°$). The images were taken from the STScI Digital Sky Survey and were scaled to 1″.5 pixel^{-1}. For each of the fields, we examined the number of stars present using the DAOPHOT program to find and count stars. The average star count of the two reddened fields was 260 stars, for the two unreddened stars CPD $-65°249$ (No. 11) and CPD $-71°252$ (No. 31) it was 340 stars, and for the "empty" fields we had an average count of 426 stars. More accurate results would require deep, high S/N CCD images of the field, as these averages are very approximate owing to the bright magnitude limit of the images we worked with. Nevertheless, the preliminary results from this elementary star counting exercise support the idea that the two unreddened stars tested appear toward holes in the cloud.

We have made a revised plot of extinction and distance in Figure 4*b* by including in the plot only stars that appear toward parts of the filament where the *IRAS* 100 μm flux exceeds 1.8 MJy Sr^{-1}. As the *IRAS* 100 μm flux has been shown to be correlated with extinction (Magnani & De Vries 1986), this threshold should select those stars that appear toward regions in the sky where the filament has detectable extinction. This revision of our sample also excluded stars 1–4, which appear toward a different cloud at the extreme eastern edge of the region shown in Figure 3. In Figure 4*b*, we have normalized the values of $E(B-V)$ by the *IRAS* 100 μm flux for this revised sample to give a more uniform basis for assessing the increase in reddening as a function of radial distance. Since our stars appear toward portions of the cloud with wide ranges of dust column density and emissivity, the normalization gives greater sensitivity to the mean reddening as a function of distance.

We see in Figure 4*b* a much clearer trend in $E(B-V)$, with a significant increase in $E(B-V)$ at $d \geq 110$ pc. One value in Figure 4*b* that appears at $d = 230$ pc has a low value of $E(B-V)/I_{100\mu}$, corresponding to the star CPD $-74°277$, which has the largest value ($I_{100\mu} = 4.08$ MJy Sr^{-1}) in our entire sample. This large value of $I_{100\mu}$ could be the result of an embedded source in the cloud, or perhaps an unresolved *IRAS* point source. To check this possibility, we searched the SIMBAD catalog near this star, and have indeed verified that only 3′ from CPD $-74°277$ is the radio source PMN J0349-7433 reported in the new Parkes-MIT-NRAO Survey (Wright et al. 1994). Further observations are planned to more precisely determine the nature of this source and its connection to the filament.

The uncertainties in photometric distance determinations

TABLE 3

DISTANCES AND MEASURED $E(B-V)$ FOR UNREDDENED STARS WITH SPECTRAL TYPES IN THE LITERATURE

Star	V	Spectral Type[a] (Lit.)	$E(B-V)$[b] (Lit.)	Spectral Type (Phot.)	$E(B-V)$ (Phot.)	D[b] (Lit.)	D (Phot.)	D[c] (*HIPPARCOS*)
HD 17981.....	8.4	A9	0.05	A9.5	0.01	111	114	357
HD 20966.....	7.4	A4	0.06	A3	0.05	95	104	106
HD 21115.....	7.3	A9	0.06	F0	0.0	66	68	86
HD 22449.....	7.55	A3.5	0.04	A2.5	0.05	109	117	151
HD 22488.....	7.5	Ap...	...	A9	0.08	...	70	207
HD 23509.....	7.8	A5	0.17	A7.5	0.07	90	89	214
HD 25938.....	6.59	A1.5	0.035	A1.5	0.02	85	87	101
HD 27346.....	6.99	A9	0.054	A9.5	0.04	58	57	115
HD 29769.....	7.0	A6	0.034	A5.5	0.05	71	72	148

NOTE—"Phot." refers to a quantity based on the photometric spectral classification.

[a] Spectral type from the SIMBAD database.

[b] Derived with photometry from present work, and spectral type from the SIMBAD database.

[c] Distance calculated using parallax data from *HIPPARCOS* satellite.

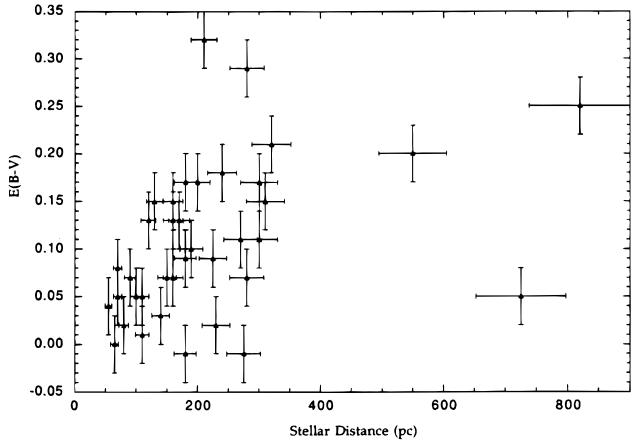

FIG. 4*a*

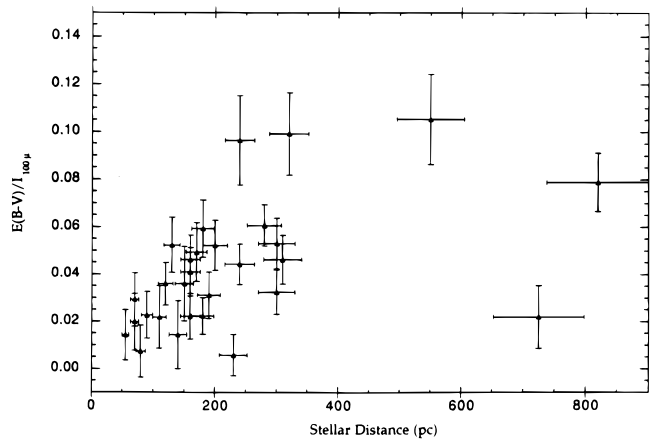

FIG. 4*b*

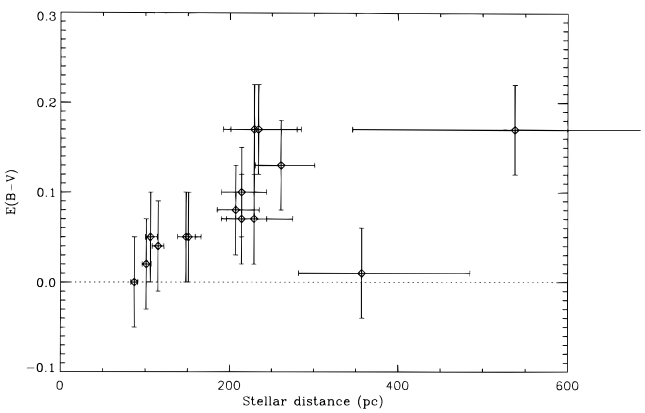

FIG. 4*c*

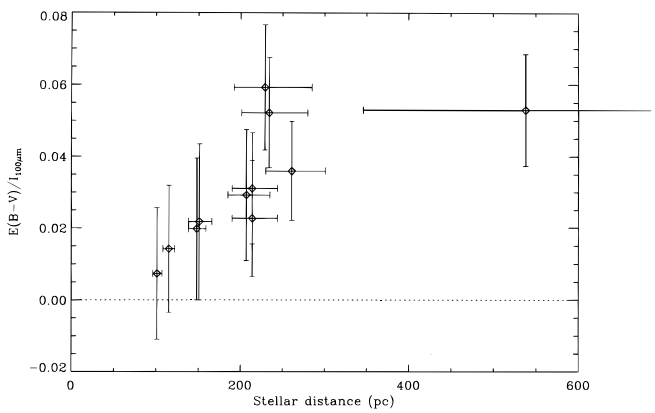

FIG. 4*d*

FIG. 4.—(*a*) Plot of the measured color excess $E(B-V)$ against the distance to the star for our sample as derived from photometric spectral classification. (*b*) The same plot as (*a*), but including only stars with $I_{100\mu} > 1.8$ MJy Sr^{-1} and normalized to $E(B-V)/I_{100\mu}$ to account for variations in the cloud thickness. The plots shows several points that are unreddened at distances $d \leq 110$ pc, and an abrupt increase in the average $E(B-V)$ for $d > 110$ pc. The measured average value of $E(B-V) = 0.18$ for the stars with $d > 110$ pc. (*c*) Using *HIPPARCOS* trigonometric parallax data, the same plot as in (*a*), but for our subsample of 15 stars with the more reliable *HIPPARCOS*-derived distances. The rise in $E(B-V)$ is clear in this figure, but at a revised distance of $d \geq 200$ pc. (*d*) The same plot as in (*b*), but for the 15 stars with *HIPPARCOS*-derived distances. A similar smooth rise in $E(B-V)/I_{100\mu}$ is seen at $d \geq 200$ pc.

are large, and the distances shown in Figures 4*a* and 4*b* are almost definitely underestimates of the actual stellar distances. The recent release of the *HIPPARCOS* satellite has allowed us to determine trigonometric parallax distances for a subset of the nearest and brightest stars in our sample. These 15 stars with *HIPPARCOS* parallax data are shown in Figures 4*c* and 4*d*, which plot $E(B-V)$ and $E(B-V)/I_{100\mu}$, respectively, against distance. The values of distances and uncertainties are indicated on the plots, and the distance estimates are included in Tables 2 and 3. In Figure 4*c*, we also see a rising trend in $E(B-V)$ with distance, with the first reddened stars appearing at distances of $d > 220$ pc. Figure 4*d* has been prepared with the same threshold of *IRAS* $I_{100\mu}$ as Figure 4*b*, and shows a cleaner signal rising steadily for stars with $d > 200$ pc.

From the interpretation of Figure 4, we conclude that the photometry appears to detect significant extinction arising from the cloud toward stars at distances of $d \geq 200$ pc, and shows a range in $E(B-V)$ values from $0.1 \leq E(B-V) \leq 0.2$ for stars appearing in the dense parts of the cloud with $I_{100\mu} \geq 1.8$ MJy Sr^{-1}. The greater reliability of the *HIPPARCOS* distances over the photometric distance estimates causes us to rely more heavily on the rise in $E(B-V)$ shown in Figures 4*c* and 4*d*, even if it is based on a smaller sample of stars.

For nearby stars with little or no observed color excess, the distances of the stars becomes critical to providing a lower limit for the distance of the cloud. In Table 3 we present the spectral types available from SIMBAD for the stars that appear in the foreground of the cloud based on Figure 4. We examine this sample of nearby stars further to test the reliability of the photometric classification and to compare the accuracy of spectroscopic parallaxes against *HIPPARCOS* parallaxes. All the stars in the control sample have reported spectral types from SIMBAD with luminosity classes of V or IV/V. We find that the spectral types from SIMBAD agree extremely well with our photometric spectral types; in most cases the resulting derived distances to the unreddened stars agree to within 5%–10%. However, the *HIPPARCOS* data clearly shows that while photometrically derived distances in many cases agree well with the actual distances, photometric distance determinations are prone to underestimating many distances by factors of 2 or more because of the unknown luminosity class of the star.

Based on the stellar distances reported in Table 3, and assuming that the *HIPPARCOS* distances are accurate, we adopt a lower limit to the cloud distance of $d > 200$ pc, which is the lower limit of distance at which we detect significant photometric reddening of stars.

We should also note that this lower limit for the distance is consistent with the detection of the white dwarf LB 1663 in the vicinity of the filament in the EUV, which suggests that the region near the filament is devoid of ISM out to the white dwarf distance of 103 pc (Wang & Yu 1994).

3.3. Ca II K *Absorption Line Results*

To study the kinematics and column densities of the cloud, and to derive upper limits to the distance of the cloud, we have obtained high-resolution spectra for two of the brightest and hottest stars that appear toward dense parts of the filament. The two stars chosen are HD 22252 and HD 26109, No. 8 and 23 in Figure 3. The MK spectral types of the stars were combined with the measured magnitudes and color excesses to estimate the distances of the stars, which are listed in columns 4 and 5 of Table 4.

The observed spectra for the two stars in Table 4 are presented in Figure 5. For each detected component, the modeled values of component velocity, *b*-value, and column density are presented in columns 6, 7, and 8 of Table 4. The modeled line profiles are also superimposed on the observed line profiles, and appear as dashed line in Figure 5.

Interstellar Ca II K absorption lines were detected for both the HD 26109 and HD 22252 sight lines. The two detected absorption lines have strikingly different line profiles. For the star HD 26109, interstellar absorption appears in a single unresolved component and ranges in LSR velocity from -8 to $+8$ km s^{-1}. The total column density of Ca II for HD 26109 was measured at $N_{\rm Ca\,II} = 1.14 \times 10^{12}$ cm^{-2}, based on the modeled single component at $v_{\rm LSR} = 3.8$ km s^{-1}.

The star HD 22252 shows a very different structure, appearing in Figure 5 to have three components ranging in LSR velocity from -12 to $+16$ km s^{-1}. The total column density of Ca II in the HD 22252 sight line estimated from averaging our two spectra is 1.53×10^{12} cm^{-2}, slightly higher than the total Ca II column density toward HD 26109. The increased $N_{\rm Ca\,II}$ toward HD 22252 could be due to enhanced values of $N_{\rm Ca\,II}/N_{\rm Ca\,I}$ arising from a kinematic disruption of the cloud.

Further observations of HD 22252 at higher resolution ($\lambda/\delta\lambda = 132{,}000$) were obtained to resolve the actual number of absorption components in the sight line. The observed high-resolution spectrum is presented in Figure 6.

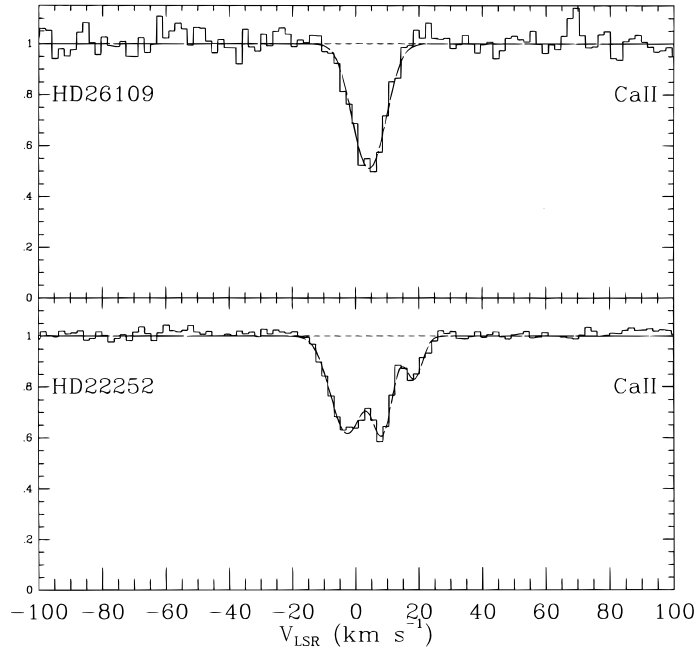

FIG. 5.—Plot of the Ca II absorption line spectra for the stars HD 26109 and HD 22252. The total column densities of Ca II are nearly identical for the two sight lines, but very different kinematics are observed from the cloud, with more than three components visible in the HD 22252 spectrum.

The modeled profile to the data in Figure 6 includes seven cloud components, and is superimposed on the data of Figure 6 as a dashed lines. The results of the cloud models are presented in the lower half of Table 4. It is clear from Table 4 that both the velocity scales and the total column densities for the HD 22252 observations match, with the improved resolution allowing for a more complete picture of the kinematic structure of the cloud. We have included both observations to help illustrate the importance of using the highest dispersion observations in obtaining information on interstellar kinematics.

Three clouds in our HD 22252 line profile model have *b*-values close to the minimum resolvable value of half the instrumental half-width. The narrowest components are seen at velocities close to $v_{\rm LSR} = 0$ km s^{-1}, and modeled *b*-values of only 1.3, 2.0, and 1.2 km s^{-1} are found for the components at $v_{\rm LSR} = 0.7$ km s^{-1}, $v_{\rm LSR} = 4.9$ km s^{-1}, and $v_{\rm LSR} = 8.6$ km s^{-1}, respectively. The maximum observed

TABLE 4

LINE PROFILE MODELING RESULTS FOR Ca II K ABSORPTION

Star Name (1)	Spectral Type[a] (2)	V (3)	$E(B-V)$ (4)	Distance (pc) (5)	$V_{\rm LSR}$ (6)	b (km s^{-1}) (7)	$N_{\rm Ca\,II}$ (cm^{-2}) (8)
HD 22252.....	B6V	5.81	0.13	260	−3.1	6.4	8.34×10^{11}
...	...	...	...	...	8.0	3.2	5.20×10^{11}
...	...	...	...	...	18.0	2.7	1.71×10^{11}
HD 26109.....	B9.5V	8.54	0.17	200	3.8	6.2	1.14×10^{12}
HD 22252.....	B6V	5.81	0.13	260	−8.0	3.45	2.33×10^{11}
...	...	...	...	...	−3.7	2.22	2.82×10^{11}
...	...	...	...	...	0.7	1.28	2.51×10^{11}
...	...	...	...	...	4.9	1.98	1.47×10^{11}
...	...	...	...	...	8.6	1.15	4.3×10^{11}
...	...	...	...	...	18.6	3.50	1.58×10^{11}
...	...	...	...	...	14.9	2.33	5.41×10^{10}

[a] Spectral types taken from the SIMBAD database.

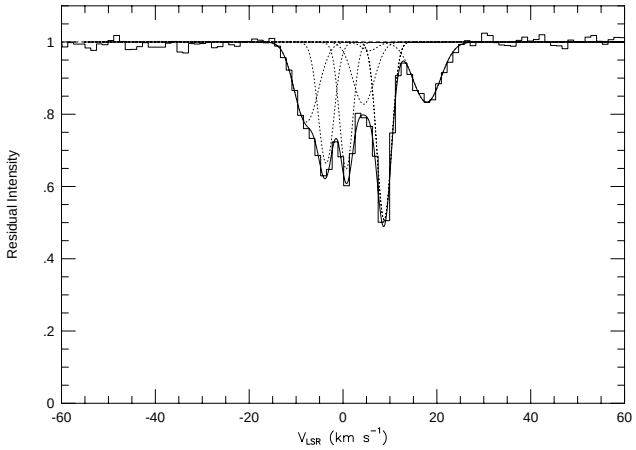

FIG. 6.—The high-resolution Ca II K spectrum of HD 22252 with the results of the profile fitting program, which matches the data best with a model including seven components. The absorption for the HD 22252 ranges from $v_{LSR} = -12$ km s^{-1} to $v_{LSR} = +16$ km s^{-1}, and is formed from warmer and disrupted gas on the high galactic latitude side of the filament. The resulting values of N, b, and v_{LSR} are presented in Table 4.

b-value, on the other hand, is 3.5 km s^{-1} for the highest velocity component at $v_{LSR} = 18.6$ km s^{-1}. The observed b-values are consistent with the hypothesis that our spectrum is detecting both quiescent components and several components that have been shocked into motion and heated in the process.

The observation of additional structure in the HD 22252 sight line at higher resolution is consistent with other recent explorations in very high resolution spectroscopy that show additional components of interstellar absorption with resolved b-values of $b = 1$ km s^{-1} (Hobbs & Welty 1991; Barlow et al. 1995). It is impossible to discern any difference in line-of-sight distances between the different components revealed in the spectrum of Figure 6 from our limited observations. It does seem likely, however, that they all arise from the same filament, since the two stars HD 26109 and HD 22252 are both at comparable distances and appear toward comparably bright ($I_{100\mu} > 3.2$ MJy Sr^{-1}) parts of the filament.

The large difference in component velocity and width within the HD 22252 spectrum raises the possibility that the cloud may contain coexisting gas at two very different temperatures or at two very different levels of bulk turbulent motion. We can estimate upper limits to the cloud temperatures from the observed b-values. The line widths in reality are a function of both thermal and turbulent motions in the clouds, and upper limits of T_{kin} are calculated by matching the observed broadening with the random thermal velocities expected at $T_{cloud} = T_{kin}$. Our estimated upper limits to the cloud temperatures range from $T_{cloud} \leq 3400$ K for the component at $v_{LSR} = 8.6$ km s^{-1} with $b = 1.2$ km s^{-1} to $T_{cloud} \leq 30000$ K for the components at $v_{LSR} = -8.04$ km s^{-1} and $v_{LSR} = 18.56$ km s^{-1} with $b = 3.5$ km s^{-1}. These upper limits to the cloud temperature, while very high, provide a basis for comparison with line widths in other species to determine the relative contributions of thermal and turbulent motions in the cloud.

3.4. Na I D *Absorption Line Results*

To further explore variations in kinematics within the cloud and to obtain improved information about the line widths within the cloud, we have observed nine stars at CTIO with the echelle spectrograph to detect absorption in the Na I D lines from the interstellar material. The results of these observations are presented in Figure 7 and Table 5. We have obtained detections for seven of these nine stars, which show strong absorption in Na I D from $v_{LSR} = 0$ km s^{-1} to $v_{LSR} = 10$ km s^{-1}. In all cases, the Na I D absorption is confined to a narrower range of velocities than the Ca II absorption, and no significant trend is seen in the Na I velocities from one end of the cloud to the other, as is possibly detected in H I emission (McGee et al. 1986). Our Na I D lines are in many cases saturated, and therefore accurate determinations of column density and component structure are difficult at this resolution. The simultaneous fitting of D1 and D2 lines places some constraints on the b-values, however, and we are able to determine that the b-values for the Na I components in the sight line are well below our instrumental resolution of 4.2 km s^{-1}. With the profile models, we predict b-values in most cases in the

TABLE 5

LINE PROFILE MODELING RESULTS FOR Na I D ABSORPTION

Star Name (1)	Spectral Type (2)	V (3)	$E(B-V)$ (4)	Distance[a] (pc) (5)	V_{LSR} (6)	b (km s^{-1}) (7)	$N_{Na\,I}$ (cm^{-2}) (8)
HD22449.....	A2.5V	7.53	0.05	>150	...	...	$<2.0 \times 10^{10}$
HD26594.....	A2.5V	8.97	0.17	>230	1.1	3.1	4.68×10^{12}
...	...	...	...	...	6.7	0.8	1.18×10^{12}
HD29769.....	A5.5V	7.01	0.05	>260	5.4	3.8	1.10×10^{12}
HD25938.....	A1.5V	6.6	0.02	>100	9.9	1.1	2.85×10^{12}
HD26109.....	A0.0V	8.6	0.17	>230	4.6	3.4	2.36×10^{13}
HD22488.....	A9.0V	7.5	0.08	>200	8.8	3.2	3.74×10^{12}
HD23509.....	A5.0V–A7.5V	7.8	0.07–0.15	>215	−0.6	6.0	7.18×10^{11}
...	...	...	...	...	0.2	5.2	4.87×10^{11}
...	...	...	...	...	8.8	2.0	5.21×10^{12}
...	...	...	...	...	19.2	1.5	8.40×10^{12}
HD22252.....	B6.0V	5.8	0.13	>260	−2.0	4.8	1.18×10^{12}
...	...	...	...	...	6.0	2.1	9.78×10^{12}
HD22634.....	A3V	6.75	...	110[b]	...	...	$<2.0 \times 10^{10}$

[a] Distance estimates based on *HIPPARCOS* parallaxes unless otherwise indicated.
[b] Distance based on photometric classification.

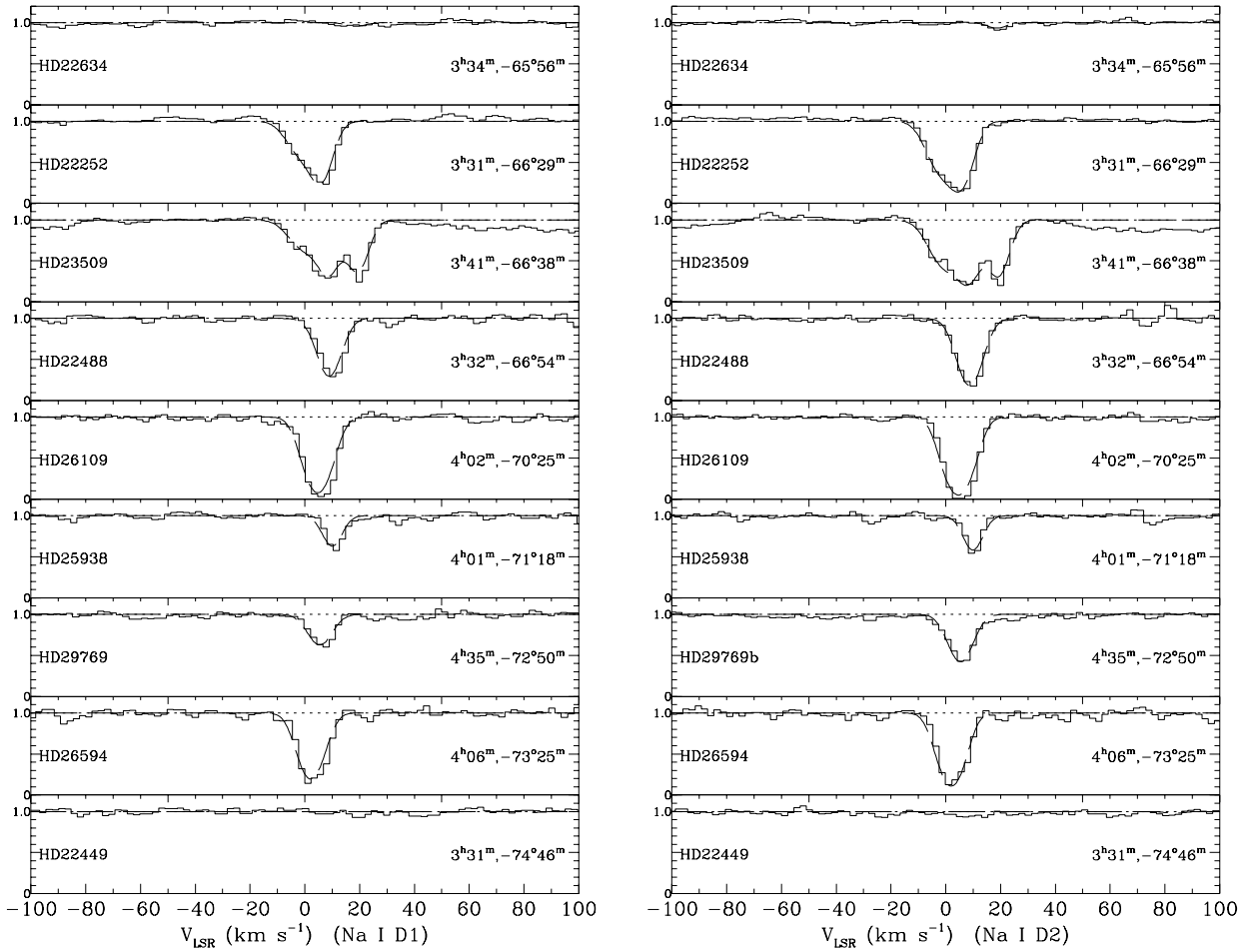

FIG. 7.—Plot of the Na I D absorption line spectra for the stars within the region shown in Fig. 3. The stars are sorted by declination, and are presented in order from north to south as seen in Fig. 3. Detections of Na I are seen in seven of the stars, and five of these have strong Na I D absorption at the cloud velocity of $v_{\rm LSR} = 5.0$ km s^{-1}. These stars are used to constrain the upper limit of distance to the cloud, as discussed in § 3.5. The two panels present the data and line profile fits for D1 and D2 components, which were fit simultaneously. The results of the fits are presented in Table 5.

range $1.0 < b < 3.5$ km s^{-1}, consistent with the higher dispersion Ca II results for HD 22252.

The largest column density Na I D components typically exceed 5×10^{12} cm^{-2}, and occur at an average velocity of $v_{\rm LSR} = 5.5$ km s^{-1}. This velocity corresponds well with the average velocity of the 21 cm H I emission reported by McGee et al. (1986), and therefore is almost certainly a strong detection of filament in absorption. Four of our stars, HD 26594, HD 26109, HD 23509, and HD 22252, show strong Na I D absorption (defined as total $N_{\rm Na\,I} > 5 \times 10^{12}$ cm^{-2}); these stars have derived distances of 180, 200, 215, and 260 pc, respectively. Of these four background stars, HD 23509 and HD 22252 alone have *HIPPARCOS* parallaxes, and their distances of 215 and 260 pc form the best estimate for the upper limit of the cloud distance. Strong absorption is also seen toward the star HD 22488, which has a total $N_{\rm Na\,I} = 3.7 \times 10^{12}$ cm^{-2} and a distance of 207 pc, based on the *HIPPARCOS* trigonometric parallax. Surprisingly, two stars within this group of strong Na I D absorbers are unreddened, with $E(B-V) = 0.07$ for HD 23509, and $E(B-V) = 0.08$ for HD 22488.

In summary, our detection of strong absorption toward five stars allows us to strongly constrain the upper limit for the cloud distance at $d < 230 \pm 30$ pc, based on the average of the *HIPPARCOS*-derived distances for three strongly absorbing stars. The uncertainty reported is the approximate average uncertainty for the three stars, as reported in the *HIPPARCOS* catalog.

3.5. *Comparison with 21 cm Observations*

Additional temperature information for the filament can be obtained by considering 21 cm H I absorption from distant continuum sources. A recent study of 21 cm absorption by quasars in the vicinity of the LMC (Mebold et al. 1991) has observed three sources within the region of Figure 3. One of the sources, PKS 0409−752, appears near the southern edge of the filament in Figure 3, and shows two components of absorption centered at the HD 26109 spectrum absorption velocity of $v_{\rm LSR} = 3.8$ km s^{-1}. The average width of the H I absorption components from the vicinity of our filament is measured to be $\delta v = 3.4$ km s^{-1}. The two components are blended and fill a velocity width FWHM of approximately 7.0 km s^{-1}. Conservatively estimating an upper limit for the 21 cm absorption line width of $b_{\rm H\,I} < 3.5$ km s^{-1}, we can easily compute the upper limit for $T_{\rm kin}$ as $T_{\rm kin} < 750$ K.

The average spin temperature calculated for the resolved galactic 21 cm H I absorption spectra is also reported to be $\langle T_{\rm sp} \rangle = 500$ K, which can provide an important lower limit for the kinetic temperature of the gas if the 21 cm absorption spectra are of sufficient resolution to resolve the component structure within the sight line. Combining the

temperature constraints for the filament, we determine that $500 < T_{\rm kin} < 750$ K. The much higher upper limit for $T_{\rm kin}$ derived from the Ca II line widths suggests that either the majority of the motions in the Ca II detected in the cloud result from bulk turbulent motions, or that the Ca II spectra are not fully resolving the velocity structure of the absorbing components.

Since, as we argued in § 3.3, we expect Ca II to have resolved the component structure in the cloud, we can use our result to estimate the amount of broadening that results from turbulent motions. If we adopt $b_{\rm thermal} < 0.56$ km s^{-1} for the Ca II gas, which corresponds to the resulting broadening for gas at $T_{\rm kin} = 750$ K, we can compute the resulting turbulent broadening $b_{\rm turb}$, since the broadening should add in quadrature. Our resulting values of $b_{\rm turb}$ range from $b_{\rm turb} \geq 1.06$ km s^{-1} for the component at $v_{\rm LSR} = 8.6$ km s^{-1} with $b = 1.2$ km s^{-1} to $b_{\rm turb} \geq 3.45$ km s^{-1} for the components at $v_{\rm LSR} = -8.04$ km s^{-1} and $v_{\rm LSR} = 18.56$ km s^{-1} with $b = 3.5$ km s^{-1}.

An alternative explanation is that the Ca II is not well mixed with the H I responsible for the 21 cm absorption lines, and that the two absorption lines sample gas at very different kinetic temperatures. While this may be possible, the very narrow 21 cm H I absorption line shows no hint of absorption by gas with Doppler values $b \geq 3.5$ km s^{-1}, and it seems unlikely that the Ca II would exist in clouds without detectable 21 cm absorption. Since ionization potentials $\chi_{\rm Ca\,I} = 6.1$ eV, and $\chi_{\rm Ca\,II} = 11.9$ eV, the Ca II is expected to be surrounded by large amounts of H I.

We observe that since the 21 cm absorption lines should provide a complete sampling of neutral gas in the sight line, they can also be used to rule out the existence of additional components at either higher velocities or larger b-values. The quasar 21 cm H I absorption velocities agree very well with our optical Ca II absorption velocities. Since no additional 21 cm absorption components are observed toward the filament, we have additional assurance that we have indeed detected the filament in absorption, and that only trace amounts of H I can exist at higher velocities (and presumedly greater distances) than those detected in our program stars. For example, the optical depth limit of H I at higher velocities is reported by Mebold et al. (1991) to be $\tau < 0.008$ for the source PKS 0409−752, which strongly suggests that the filament is a local, cool shell of gas, with $d < 260$ pc, the distance of the program star HD 22252.

3.6. *Distance and Size of the IR filament*

Using the photometric distance estimate of $d \geq 215$ pc from § 2.1 as the lower distance estimate to the cloud and the distance $d \leq 260$ pc of HD 22252 as a definite upper limit, we adopt the value of $d = 230 \pm 30$ pc for the cloud, which reflects the average distance of the strongly absorbing stars and includes the uncertainty estimate from the *HIPPARCOS* parallax data.

We can combine this estimate with the measured angular size of the filament to determine the linear sizes of the infrared features. The width of the filament ranges from 90′ to 200′ in the IR image of Figure 3, corresponding to a thickness of 6.0 to 13.4 pc at the adopted distance of the cloud. The angular length of the filament appears to be over 20°, corresponding to a length of over 90 pc for the cloud. Within the larger arc of the filament are a number of smaller, bright condensations. These knots of intense 100 μm *IRAS* emission were measured to have angular sizes of 4′.5 to 23′, corresponding to linear dimensions of 0.30 to 1.50 pc at the adopted distance of the cloud.

We can also determine the approximate center of the circular part of the filament shown in Figure 3. Using a fit to the locus of points with $I_{100\mu} \geq 1.8$ MJy Sr^{-1}, we have estimated the location of the center of the filament. The center was determined to be near the coordinates $\alpha(1950) = 2^{\rm h}40^{\rm m}00^{\rm s}$, $\delta(1950) = -72^{\rm d}00^{\rm m}00^{\rm s}$, corresponding to galactic coordinates of $l = 291.6$, $b = -42.8$.

To determine whether the filament was formed from a recent supernova, we have searched the COMPTON-EGRET gamma-ray source catalog (Fichtel et al. 1993) to determine whether any detected gamma-ray sources appear near our calculated center coordinates. From a search of the catalog, we have determined that no sources exist within 20° of the center of the filament. Examination of the current *ROSAT* all-sky maps did show the hint of an X-ray ring at the location of our filament (W. Chen 1995, private communication), but improved maps are needed to unambiguously detect such a feature.

The galactic coordinates of our filament place it near the boundary of the β CMa tunnel ($l = 230$, $b = -15$), a region devoid of interstellar medium discovered from absorption line observations (Welsh et al. 1994). Recent observations have suggested that the void in CMa could have been formed by a local supernova, such as the one that created the Geminga pulsar (Welsh 1991). Considering the age estimate for the Geminga pulsar of $\sim 3 \times 10^5$ yr (Gehrels & Chen 1993), the supernova remnant would be expected to be in the late isothermal expansion phase, according to a standard evolutionary scenario (Spitzer 1978). We would expect for a supernova remnant of age $\sim 3 \times 10^5$ yr a diameter of $D \leq 40$ pc, using the standard supernova parameters from Spitzer (1978). However, it is thought that the average density in the local interstellar medium was very low, which would decrease resistance to the expanding remnant and could lead to the formation of a structure larger than $D = 40$ pc (W. Chen 1995, private communication). If the filament is an old SNR, it could comprise decelerating debris swept from the CMa region by the supernova shock wave as the filament decelerated to its present velocity. Further observations are needed to confirm this interesting possibility.

3.7. *Variations in IRAS Colors within the Filament*

To further examine conditions in the filamentary clouds, we have analyzed images for the region from the latest *IRAS* sky survey, the Infrared Sky Survey (ISSA). The ISSA plates were flattened, using algorithms described elsewhere, to remove the zodiacal backgrounds (Penprase & Helou 1997). For the sight lines of each of our 38 program stars, we extracted the *IRAS* fluxes and derived estimates of the colors $R(12, 100)$, $R(60, 100)$, and $R(12, 25)$, ratios of the *IRAS* emission for the two bands specified. The results of the *IRAS* fluxes and colors are presented in Table 6. Infrared colors for HD 22252, or HR 1092, have been reported in the literature (Gaustad & Van Buren 1994), and agree well with our values in Table 6. For HD 22252, we calculate $R(12, 100) = 0.08$, and $R(60, 100) = 0.22$, which compare well with the values $R(12, 100) = 0.06$ and $R(60, 100) = 0.32$ from Gaustad & Van Buren (1994).

For the ISSA plate shown in Figure 3, we have also prepared a color summary plot, consisting of gray-scale two-dimensional histograms of the *IRAS* color ratios within the

TABLE 6

IRAS FLUXES AND COLORS TOWARD PROGRAM STARS

Number (1)	Star Name (2)	$I_{12\mu}$ (3)	$I_{25\mu}$ (4)	$I_{60\mu}$ (5)	$I_{100\mu}$ (6)	R(12, 100) (7)	R(60, 100) (8)	R(12, 25) (9)
1	HD 17419	0.29	0.48	0.43	2.28	0.13	0.19	0.60
2	HD 17732	0.26	0.32	0.26	1.50	0.17	0.17	0.81
3	HD 17901	0.28	0.31	0.27	1.63	0.17	0.16	0.90
4	HD 17981	0.33	0.50	0.14	1.00	0.33	0.14	0.66
5	HD 20966	0.19	0.03	0.17	1.41	0.14	0.12	6.06
6	HD 21115	0.29	0.03	0.16	1.55	0.18	0.10	9.70
7	HD 22218	0.15	0.17	0.26	2.09	0.07	0.12	0.89
8	HD 22252	0.27	0.19	0.81	3.62	0.08	0.22	1.41
9	HD 22449	0.30	0.21	0.38	2.30	0.13	0.17	1.44
10	CPD −65°249	0.06	0.04	0.19	1.78	0.03	0.11	1.28
11	HD 22488	0.18	0.13	0.42	2.74	0.07	0.15	1.42
12	CPD −75°239	0.22	0.19	0.47	3.17	0.07	0.15	1.18
13	HD 23334	0.00	0.13	0.16	1.64	0.00	0.10	0.03
14	HD 23509	0.16	0.13	0.36	3.09	0.05	0.12	1.26
15	CPD −67°248	0.22	0.10	0.57	3.22	0.07	0.18	2.16
16	CPD −74°277	0.33	0.30	0.59	4.08	0.08	0.14	1.12
17	CPD −66°227	0.02	0.13	0.31	2.12	0.01	0.15	0.19
18	HD 25027	0.43	0.60	0.62	3.25	0.13	0.19	0.71
19	HD 25224	0.39	0.43	0.48	3.18	0.12	0.15	0.91
20	CPD −70°268	0.43	0.54	0.72	4.05	0.11	0.18	0.79
21	HD 25863	0.34	0.31	0.68	4.79	0.07	0.14	1.08
22	HD 25938	0.41	0.59	0.56	2.73	0.15	0.20	0.70
23	HD 26109	0.50	0.57	0.68	3.26	0.15	0.21	0.87
24	CPD −68°242	0.13	0.11	0.26	1.72	0.08	0.15	1.22
25	CPD −72°278	0.40	0.44	0.52	3.41	0.12	0.15	0.91
26	HD 26433	0.31	0.36	0.42	2.64	0.12	0.16	0.84
27	HD 26594	0.31	0.40	0.51	2.87	0.11	0.18	0.77
28	HD 26541	0.44	0.49	0.58	3.25	0.14	0.18	0.90
29	HD 26668	0.15	0.07	0.10	0.88	0.18	0.12	2.30
30	HD 27143	0.41	0.55	0.55	3.17	0.13	0.17	0.75
31	CPD −71°252	0.41	0.54	0.53	3.46	0.12	0.15	0.76
32	HD 27346	0.55	0.59	0.64	2.82	0.20	0.23	0.93
33	HD 27503	0.31	0.39	0.31	1.90	0.16	0.16	0.78
34	HD 270501	0.27	0.26	0.18	1.87	0.15	0.10	1.05
35	HD 28722	0.39	0.49	0.55	3.21	0.12	0.17	0.78
36	HD 29769	0.29	0.26	0.33	2.53	0.11	0.13	1.12
37	HD 29921	0.37	0.43	0.45	2.87	0.13	0.16	0.84
38	HD 30580	0.28	0.19	0.24	1.95	0.14	0.13	1.49

NOTE.—All fluxes in columns 3–6 are in units of MJy Sr^{-1}.

filament. The number of pixels in the filament at a given color combination determines the brightness of the pixel in the color summary plot, and the locations in the x-y plane correspond to a logarithmic scale of the *IRAS* color ratios. The color summary plot for the filament is presented in Figure 8, with the selected *IRAS* ratios indicated on the figure [for example, $R(12, 100) = I_{12\mu}/I_{100\mu}$]. An analysis of Figure 8 clearly shows that at least two and possibly three distinct populations of grains exist in the IR filament near the LMC. The mean colors of the grains are consistent with average colors of diffuse galactic cirrus, but the various populations show values that indicate significant dust grain heating. The increased values of R(12, 100) and R(60, 100) have been shown to indicate an excess of small dust grains (Desert, Boulanger, & Puget 1990) and heating in the ISM (Boulanger, Prevot, & Gry 1994).

A further analysis of spatial variations of the *IRAS* colors has been performed, and is presented in Figure 9, showing a logarithmic plot of values of R(12, 100) and R(60, 100) as a function of the y pixel coordinate of Figure 3, which approximately corresponds to declination. The vertical axis of Figure 3 also roughly corresponds to increasing galactic latitude, so the graphs in Figure 8 track the IR colors of the cloud as a function of galactic latitude. The trend in R(12, 100) and R(60, 100) clearly shows an increase in the upper high galactic end of the cloud, and mean values of R(12, 100) increase from $R(12, 100) = 0.03$ to $R(12, 100) = 0.20$ at the northern edge of the cloud. The R(60, 100) values also increase, with mean values of R(60, 100) rising from 0.10 at the southern edge of the cloud to $R(60,1\ 00) = 0.20$ at the northern high galactic latitude edge of the cloud. The decrease in R(12, 100) at the extreme edge of the cloud is also interesting, and could be explained by small grains radiating the peak of their emission at wavelengths even shorter than 12 μm.

3.8. *Spatial Variations in IRAS Emission within the Filament*

To locate precisely the sources of the enhanced values of R(60, 100) and R(12, 100), we have prepared maps of both of these *IRAS* colors, presented in Figures 10 and 11, using points in the ISSA plate that have 100 μm fluxes above the threshold of $I_{100\mu} \geq 1.8$ MJy Sr^{-1}. A map of the color temperature R(60, 100) is presented in Figure 10, showing the source for the enhanced values of R(60, 100) seen in Figures 8 and 9. A broad zone of enhanced R(60, 100) fills the central region of the cloud at $\delta = -71^{d}00^{m}$ and two "fingers" at the extreme northern (high galactic latitude) portion of the cloud. In addition, a warm isolated cloud appears to the right of Figure 10, at $\alpha = 02^{h}00^{m}$. We also present a map of the color temperature R(12, 100) for the

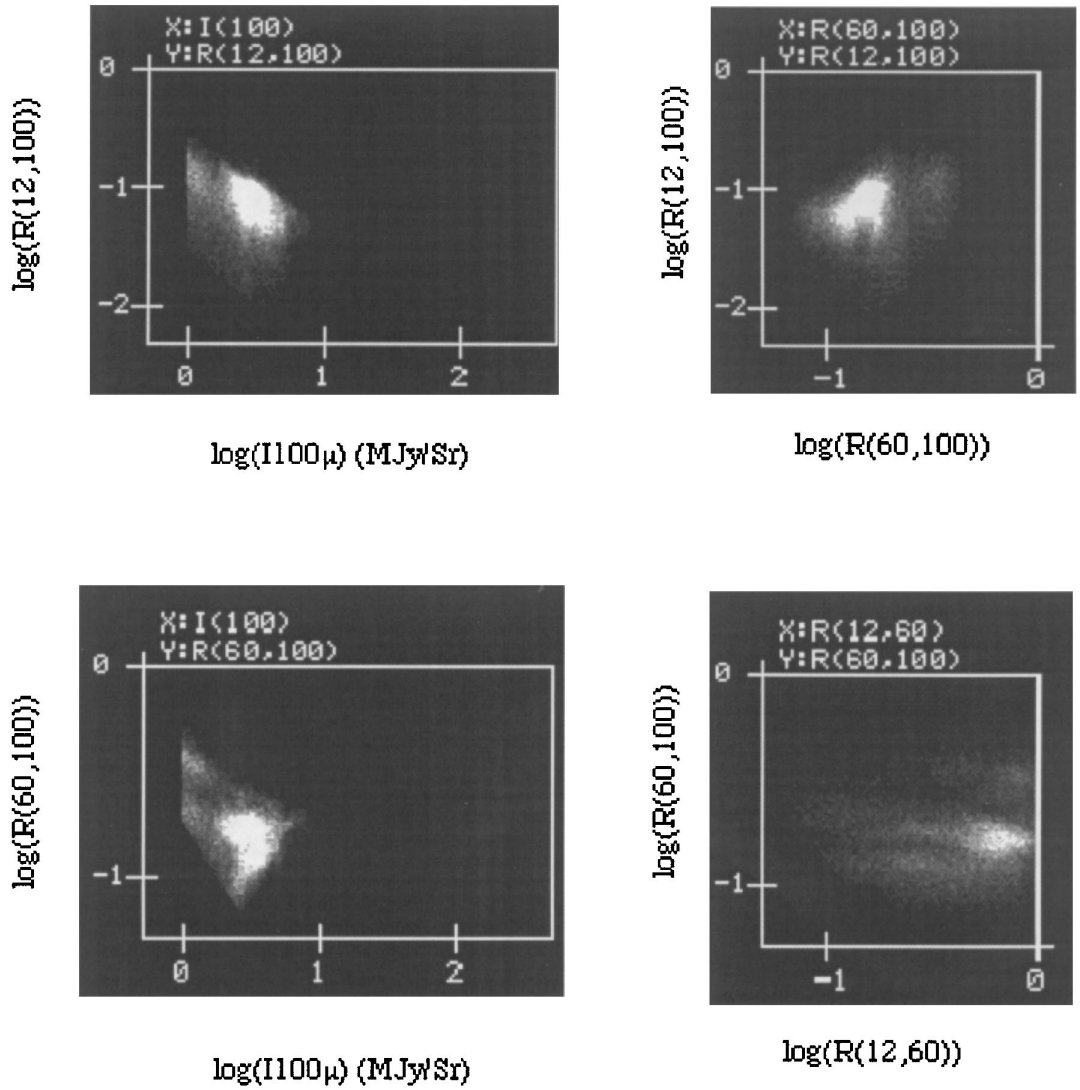

FIG. 8.—*IRAS* color-color plot for the ISSA infrared data of Fig. 3. Each panel is a two-dimensional gray-scale histogram of the *IRAS* colors for the filament. The intensity within the panel is determined by the number of pixels in the cloud with the specific *IRAS* colors corresponding to the location in the color-color plane. The ratios of four pairs of *IRAS* colors are presented in separate panels, the colors used indicated at the top of the panel. The color-color plots allow for identification of grain populations within the filament. Discrete populations are easily seen in the plot of $R(60, 100)$ and $R(12, 100)$ (*lower right*), which shows three distinct populations of grains. The plots were created from pixels with intensities above the threshold $I_{100\mu} > 1.0$ MJy Sr^{-1}. $R(60, 100)$ refers to $I_{60\mu}/I_{100\mu}$, while $R(12, 100)$ refers to $I_{12\mu}/I_{100\mu}$.

same points in Figure 11, with contours of $R(12, 100)$ drawn at $R(12, 100) = 0.08$ and $R(12, 100) = 0.12$. Figure 11 shows two zones of enhanced $R(12, 100)$ near the center of the filament and within the small isolated cloud at $\alpha = 02^{h}00^{m}$.

Figures 10 and 11 both show distinct zones within the filament with significant differences in derived *IRAS* colors. These differences could indicate distinct clouds within the sight line, or differential heating within the same filament. The filament may consist of several "strands" of clouds that are in different stages of heating from either kinematic or radiative processes.

The clearly distinct (warmer) IR colors of the isolated cloud at $\alpha = 02^{h}00^{m}$ suggests that this cloud could be a separate object from our filament, and therefore at a very different radial distance. It would be possible to argue from the *IRAS* colors that at least three and possibly four separate clouds exist within the maps of Figures 10 and 11. One possible source for the variations in *IRAS* colors could be clouds at distinct radial distances. An alternative explanation might be that the enhanced values of $R(12, 100)$ and $R(60, 100)$ in both the isolated cloud and the central and end regions of the filament arise from evolutionary processes within the same cloud, perhaps from collisions and fragmentation within the filament that are the result of kinematic processes. The extremely filamentary structure at the southern end of the cloud is especially apparent in Figure 11, where several dozen "holes" in the cloud suggest a structure of hundreds of aligned cloudlets. The flaring of the filament at the northern end also is suggestive of a filament being "stretched."

McGee et al. (1986) report a gradient of observed H I radial velocity in this southern end of the cloud, which they argue results from two separate "streams" of material. They argue that different geometries relative to our sight line and two distinct and constant space velocities result in an apparent velocity gradient. The same data, however, may also indicate an actual velocity gradient resulting from expansion of the filament in the southern end of the cloud.

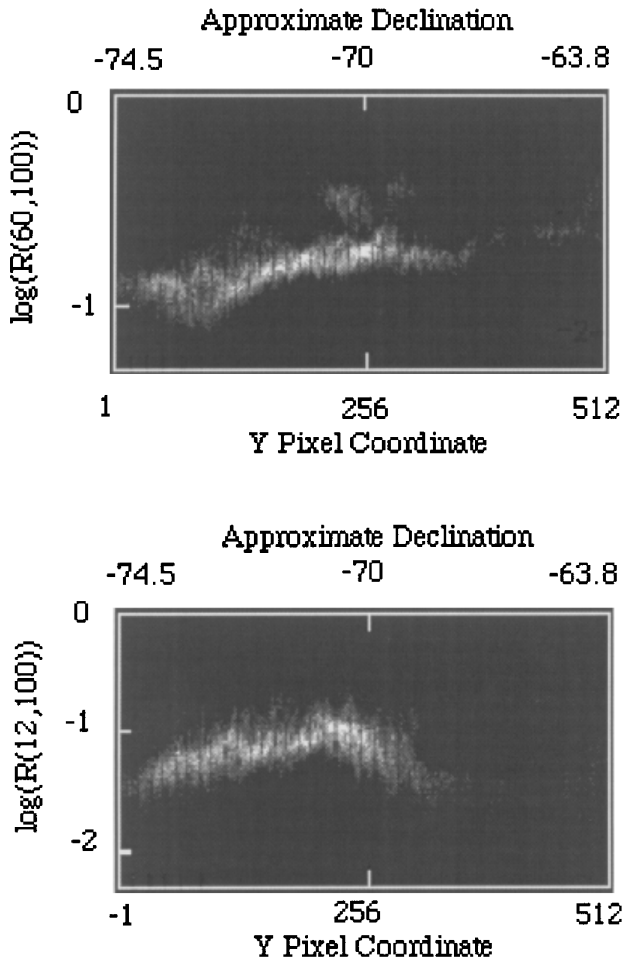

FIG. 9.—To further understand the *IRAS* colors for the region, we have plotted the infrared colors $R(12, 100)$ and $R(60, 100)$ against the y-axis coordinate of Fig. 3, approximately corresponding to a graph of the colors against both declination and galactic latitude. The dramatic increase in the mean values of $R(12, 100)$ and $R(60, 100)$ at high galactic latitudes is apparent, and is consistent with the distinct difference in the absorption line profiles of HD 26109 and HD 22252, which probe interstellar gas from either end of the filament. The increased values of $R(12, 100)$ are correlated with enhanced numbers of heated small dust grains, while $R(60, 100)$ traces the mean temperature of larger grains. The increase in both of these ratios suggests that the north high galactic latitude end of the cloud is significantly warmer and has smaller grains, both of which could be a result of shock heating or different rates of cooling from one end of the filament to the other.

This expansion could explain the increase in the number of "holes" seen in this part of the cloud, and perhaps even the isolated cloud at $\alpha = 02^{h}00^{m}$ results from this expansion.

The extremely high values of $R(12, 100)$ and $R(60, 100)$ in the central region of the filament may arise from interactions between the two "streams" proposed by McGee et al. (1986), as these points in the center of Figures 9 and 10 are very close to the boundary of the proposed streams. Some caution needs to be exercised in interpreting this region, however, since a significant background from the LMC exists, and may introduce some contaminating flux through "holes" in the filament. Further observations with higher angular resolution would be needed to determine whether the warmer *IRAS* colors in the LMC region arise from the filament or from the LMC itself. The relatively consistent velocity and column densities within the entire region of Figures 9 and 10 does, however, suggest that the filament is a single object.

4. CONCLUSIONS

From our observations of the filament near the LMC, we conclude that the object is a local shell of gas at a distance of $200 \leq d \leq 260$ pc, probably a single stream of gas that may have been released from an earlier supernova explosion. The filament extends for many degrees north of the LMC, and reaches upward to high galactic latitudes, with a linear extent of over 90 pc. The low velocity of the material and its high dust content, as revealed by the large 100 μm emission, suggests that it could be a very old supernova remnant that has cooled and decelerated. The increased *IRAS* colors $R(12, 100)$ and $R(60, 100)$ at the northern high-latitude end of the cloud are consistent with a warmer region of the cloud undergoing more rapid expansion, perhaps in response to lower pressures in the regions of higher galactic scale height $|z|$.

The Ca II line widths of the narrowest components toward HD 22252 reveal temperatures of $T_{\rm kin} \leq 3400$ K, which suggest that the Ca II gas is substantially broadened by turbulent motions. The wide range of b-values in our observed Ca II components reveals even warmer or more turbulent interstellar material, with kinetic temperatures possibly as high as $T_{\rm kin} = 30{,}000$ K. The Na I D line observations provide several independent detections of the cloud at velocities similar to those of the Ca II detections, but at generally lower b-values. Our present resolution is insufficient to allow a detailed comparison of line profiles and velocities between the Ca II and Na I D absorption. It does appear likely that the material is coexisting, however, and that the filament includes several components in both Na I and Ca II with b-values in the range $1.0 < b < 3.5$ km s^{-1}.

Since the Ca II gas is expected to coexist with Na I and H I gas, the 21 narrow cm H I absorption line widths strongly argue that the filament also contains gas which has relatively low kinetic temperatures in the range of $500 \leq T_{\rm kin} \leq 700$, and a very large and widely varying fraction of turbulent motions. This picture again suggests a model for the filament as a swarm of turbulent cloudlets that are perhaps far from pressure equilibrium with the surrounding interstellar medium. Further observations at higher resolution or with UV lines sensitive to interstellar pressure are needed to better constrain the conditions within the cloudlets.

From the analysis of the infrared emission of the cloud, at least three distinct populations of dust grains exist in the filament, and the mean dust grain temperature rises from one end of the cloud to the other. The highest temperatures in the cloud appear toward the northern high galactic latitude end, where values of $R(12, 100)$ are a factor of 10 higher and values of $R(60, 100)$ are twice those at the southern edge of the cloud.

The infrared filament of the current work presents a nearly semicircular shell of material, in many respects resembling a southern analog of the North Polar Spur. The calculated location of the center of the filament is $\alpha(1950) = 2^{h}40^{m}00^{s}$, $\delta(1950) = -72^{d}00^{m}00^{s}$. Further observations in the gamma-ray and X-ray wavelengths could detect a pulsar at the center of the filament, if the filament is indeed the result of a supernova explosion. The galactic coordinates of our filament (290, -43) place it fairly close to the β CMa tunnel, a region devoid of interstellar medium discovered from absorption line observations (Welsh et al. 1994). Recent observations have suggested that the void in CMa is the result of a nearby

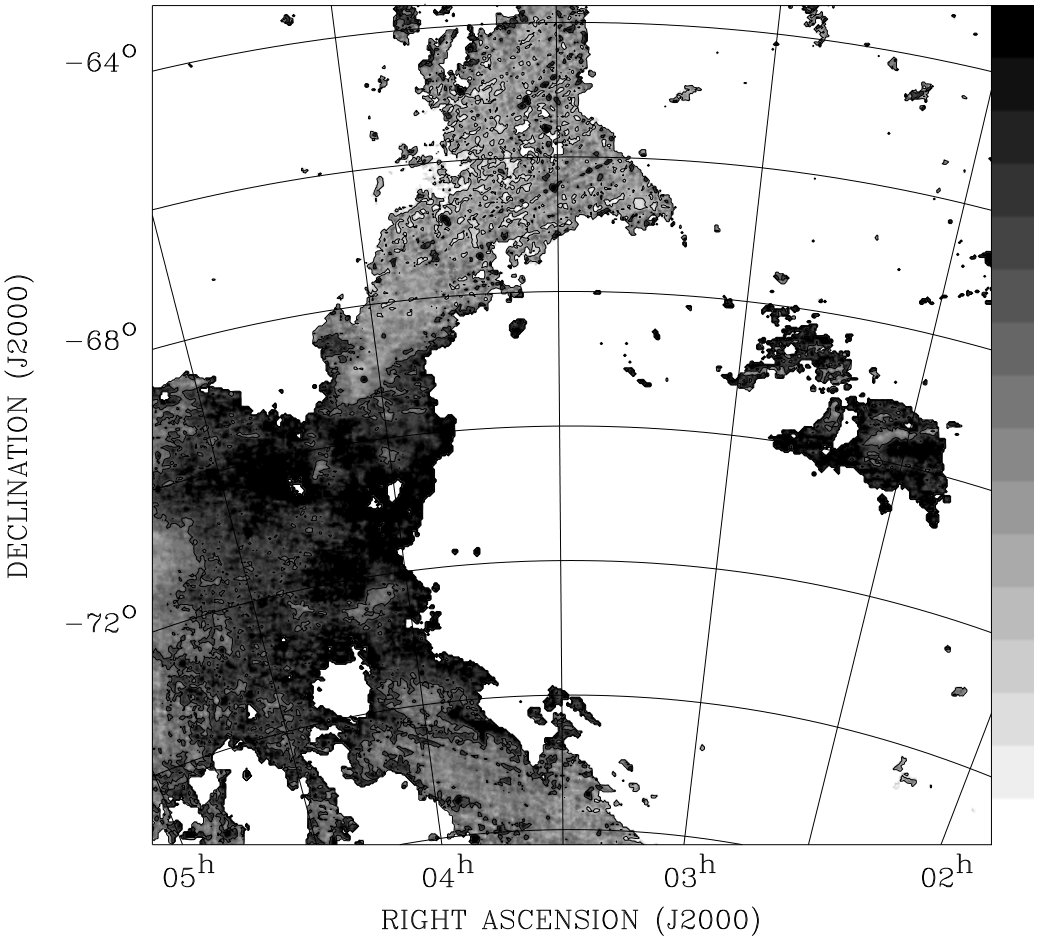

FIG. 10.—Map of the area shown in Fig. 3, using an inverted gray scale to display the values of the *IRAS* color temperature $R(60, 100)$. For this map and Fig. 11, we have applied a threshold of $I_{100\mu} \geq 1.8$ MJy Sr^{-1}. Significant increases in the value of $R(60, 100)$ are seen at the northern edge of the cloud, in the central regions near the LMC, and within a small cloudlet at the right of the figure.

supernova, and using an age estimate for the Geminga pulsar of $\sim 10^6$ yr (Gehrels & Chen 1993), it is entirely possible that the filament in the current work was ejected from this supernova.

The variety of interstellar regimes present in the cloud is hinted at in our initial observations. Further observations are needed to determine the molecular content of the cloud and the ionization ratios throughout the cloud. The observations presented here are, however, consistent with a local filament of gas in which part of the cloud is a quiescent old supernova remnant, and another part is shocked and expanding.

The interstellar medium in the foreground of HD 22252 is found from our Ca II absorption line observations to have at least seven components, with b-values ranging from $1.2 \leq b \leq 3.5$ km s^{-1}, and $N_{\rm Ca\,II}$ ranging from 1.5×10^{11} cm$^{-2} \leq N_{\rm Ca\,II} \leq 2.8 \times 10^{11}$ cm^{-2}. The width of these components rises with velocity, consistent with an interpretation of shocks heating and ionizing some of the components of the cloud. The high-resolution spectrum from the current work is expected to resolve the coolest components of Ca II absorption, but further observations at higher resolution may be needed to determine whether additional components in Na I and other neutral atoms can detect even cooler interstellar material in the cloud.

An additional result possible with the distance estimate of the present work is a derivation of the electron density of the hot component of the interstellar medium in the foreground of the filament. By using *ROSAT* PSPC observations and making the idealized assumption that the electron density and temperature in the foreground of the filament is uniform and equal to the Galactic average, it is possible to calculate a distance to the filament of 70 pc (Wang & Yu 1994). This result is highly uncertain, however, since there is no independent measurement of the electron density for the foreground region of the filament, and no clear reason why this density should be assumed a priori to be constant.

Our independent determination of the distance is more reliable, since it uses stars that are of known distances, and makes no assumptions other than that we have detected the filament in the foreground of these stars. While considerable uncertainties exist in interpreting the effects of inhomogeneities in the cloud, we believe that we have exercised great care in separating these effects by using *IRAS* thresholds, star counts, and detailed considerations of specific sight lines to determine whether stars are behind the filament. With the additional benefit of accurate, model-independent distances to 15 of our stars from the *HIPPARCOS* parallax catalog, the cloud distance appears to be well constrained from our sample.

Knowing the distance to the filament makes it possible to perform the reverse calculation and derive the average electron density of the hot component in the foreground of the

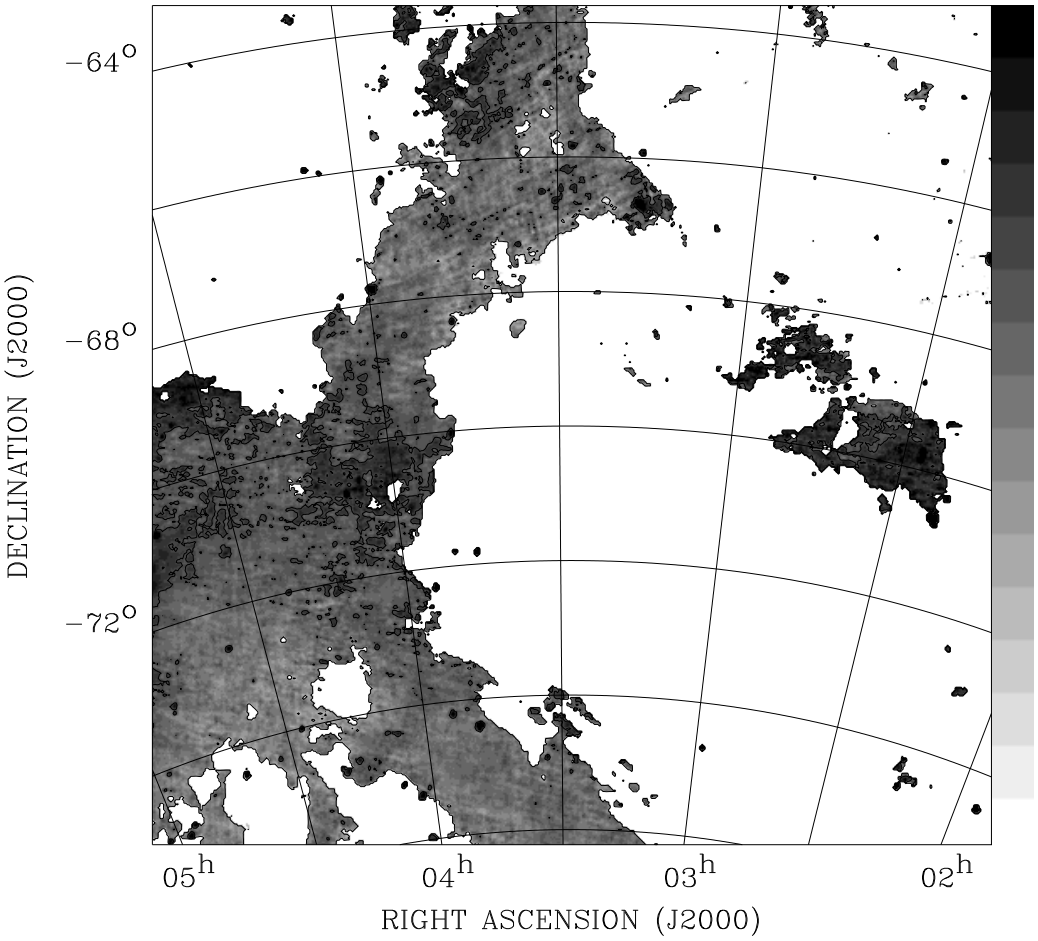

FIG. 11.—Map of the area shown in Fig. 3, using an inverted gray scale to display the values of the *IRAS* color temperature $R(12, 100)$. Significant increases in the value of $R(12, 100)$ are seen in the central regions near the LMC and within a small cloudlet at the right of the figure. Many "holes" in the filament are also clearly visible at the northern edge of the cloud, which may be the result of expansion in the filament at higher galactic latitudes.

filament based on the observed X-ray emission measure and our derived distance of 230 pc. This estimate uses the fact that the emission measure of the hot ISM varies as the square of the electron density. The revised estimate of electron density in the foreground of the filament is $n_e = 3.47 \times 10^{-3}$ cm^{-3}, substantially lower than the Galactic average of $n_e = 6.3 \times 10^{-3}$ cm^{-3}.

We would like to thank the staff of CTIO for their excellent and courteous help in working with both the 1.0 m and 1.5 m telescopes. Thanks to Robert Beswick at Pomona College for his assistance with UNIX programming, and the porting of XVOIGT to Solaris. Travel to CTIO in 1993 took place during a National Research Council postdoctoral fellowship at IPAC, and was supported by IPAC. Many of the *IRAS* analysis tools were developed in consultation with Dr. George Helou, who also sponsored the NRC fellowship of B. Penprase. We would like to thank the referee for suggesting several additions to the paper that have substantially improved its completeness. We would like to acknowledge many insightful comments from B.-G. Andersson, Uwe Herbstmeier, and Peter Wannier, who have carefully read over an earlier draft and provided many suggestions for improvements. We would like to thank Daniel Wang for his help and encouragement in the project, and for allowing the use of his IDL mapping software. We are also grateful to Pomona College for the support of faculty and student research, and for the grant to B. Penprase to travel to ESO headquarters in Garching to conduct some of the observations. Student research funds for J. Lauer and J. Aufrecht were provided by a AAS REU grant to B. Penprase. Thanks to Eliana Palazzi for help with the observations at Garching. Travel support for the CTIO observing in 1997 was provided by a NASA ADP grant to Q. D. Wang. This research has made use of the SIMBAD database, operated at CDS, Strasbourg, France. J. C. Blades provided a careful reading of the paper during the proof stage.

REFERENCES

Albert, C. E., Blades, J. C., Morton, D. C., Lockman, F. J., Proulx, M., & Ferrarese, L. 1993, ApJS, 88, 81
Barlow, M. J., Crawford, I. A., Diego, F., Dryburgh, M., Fish, A. C., Howarth, I. D., Spyromilio, J., & Walker, D. 1995, MNRAS, 272, 333
Blades, J. C., & Panagia, N. 1989, in AIP Conf. Proc. 183, Cosmic Abundances of Matter, ed. J. Waddington (New York: AIP), 406
Blades, J. C., Wheatley, J. M., Panagia, N., Grewing, M., & Pettini, M. 1988, ApJ, 334, 308
Boulanger, F., Baud, B., & van Albada, G. D. 1985, A&A, 144, L9
Boulanger, F., Prevot, M. L., & Gry, C. 1994, A&A, 284, 956
Burrows, D. N., & Mendenhall, J. A. 1991, Nature, 351, 629
Caulet, A., & Newell, R. 1996, ApJ, 465, 205
Colomb, F. R., Poppel, W. G. L., & Heiles, C. 1977, A&A, 29, 89
De Boer, K. S., Richtler, T., & Savage, B. D. 1987, ESO Workshop on the SN 1987A (Garching: ESO), 549
Desert, F. X., Boulanger, F., & Puget, J. L. 1990, A&A, 237, 215

de Vaucouleurs, G. 1960, Observatory, 80, 106
Fichtel, C. E., et al. 1993, A&AS, 97, 13
Fong, R., Jones, L. R., Shanks, T., Stevenson, P. R., & Strong, A. W. 1987, MNRAS, 224, 1059
Franco, G. A. P. 1992, A&AS, 93, 373
Frisch, P. C. 1981, Nature, 293, 377
Gaustad, J. E., & Van Buren, D. 1994, PASP, 105, 1127
Gehrels, N., & Chen, W. 1993, Nature, 361, 706
Gronbech, B., & Olsen, E. H. 1976, A&AS, 25, 213
Guo, Z., Burrows, D. N., Sanders, W. T., Snowden, S. L., & Penprase, B. E. 1995, ApJ, 453, 256
Heck, A., & Mersch, G. 1980, A&A, 83, 287
Heiles, C. 1989, ApJ, 336, 808
Heiles, C., Chu, Y. H., Troland, T. H., Reynolds, R. J., & Yegingil, I. 1980, ApJ, 242, 533
Hobbs, L. M., & Welty, D. E. 1994, ApJ, 368, 426
Luna, H. G., & Testori, J. C. 1988, A&AS, 198, 249
Magnani, L., & De Vries, C. P. 1986, A&A, 168, 271
Mar, D., & Baily, G. 1995, Proc. Astron. Soc. Australia, 12, 239
Mathewson, D. S., Ford, V. L., Schwarz, M. P., & Murray, J. D. 1979, in The Large-scale Characteristics of the Galaxy, ed. W. Burton (Dordrecht: Reidel), 547
McGee, R. X., Haynes, R. F., Grognard, J. M., & Malin, D. 1986, MNRAS, 221, 543
Mebold, U., Greison, E. W., Wilson, W., Haynes, R. F., Herbstmeier, U., & Kalberla, P. M. W. 1991, A&A, 251, L1
Mihalas, D., & Binney, J. 1981, Galactic Astronomy (San Francisco: Freeman)
Olsen, E. H. 1983, A&A, 54, 55
Penprase, B. E. 1992, ApJS, 83, 273
Penprase, B. E., & Helou, G. 1997, in preparation
Scheffler, H., & Elsasser, H. 1987, in Physics of the Galaxy and Interstellar Matter, ed. H. Scheffler (Berlin: Springer), 224
Spitzer, L. 1978, Physical Processes in the Interstellar Medium (New York: Wiley)
Wang, Q. D., & Yu, K. C. 1994, AJ, 109, 698
Wayte, S. R. 1990, ApJ, 355, 473
Welsh, B. Y. 1991, ApJ, 373, 556
Welsh, B. Y., Craig, N., Vedder, P. W., & Vallerga, J. V. 1994, ApJ, 437, 638
Wright, A. E., Griffith, M. R., Burke, B. F., & Ekers, R. D. 1994, ApJS, 91, 111
Zombeck, M. V. 1990, Handbook of Space Astronomy and Astrophysics (New York: Cambridge Univ. Press)